International Journal of Solids and Structures 000 (2018) 1–21

Contents lists available at ScienceDirect

International Journal of Solids and Structures

journal homepage: www.elsevier.com/locate/ijsolstr

Evolution of multiple Martensite variants in a SMA thick-walled cylinder loaded by internal pressure

Enrico Radi

Dipartimento di Scienze e Metodi dell'Ingegneria, Università di Modena e Reggio Emilia, Via Amendola 2, I-42122 Reggio Emilia, Italy

ARTICLE INFO

Article history:
Received 10 March 2018
Revised 6 June 2018
Available online xxx

Keywords:
Analytical solutions
Axisymmetric
Rings
Shape-memory
Thermomechanical
Cylinder
Phase transformation

ABSTRACT

The stress and deformation fields in a SMA ring or a thick-walled cylinder loaded by internal pressure at constant temperature (over the start temperature of the martensitic transformation) are determined in closed form under plane stress loading conditions. The phenomenological SMA constitutive model incorporates the volume fractions of multi-variants Martensite, which are assumed to evolve linearly with the Tresca effective stress, according to the associative flow rule and the corner flow rule. Initially, the cylinder is everywhere in a state of Austenite. The application of an internal pressure then triggers the martensitic transformation starting from the inner radius of the cylinder wall and extending towards the outer radius. If the wall thickness is large enough, the tangential stress may vanish at the inner radius and correspondingly the stress state may reach a corner of the Tresca transformation condition, thus originating two different Martensite variants according to the corner transformation rule. The admissible phase partitions within the wall thickness originating during the loading process have been systematically investigated according to the ratio between the outer and inner radii. The results obtained here suggest that the loading process should be interrupted soon after the complete martensitic transformation is achieved at the inner radius of the cylinder to avoid permanent plastic deformations.

1. Introduction

Due to their reliable performance and convenient installation, SMA couplings, fasteners and joints have been widely used for pneumatic and hydraulic connectors in aircraft and piping systems (Kapgan and Melton, 1990; Borden, 1990, 1991; Brinson and Lammering, 1993; Wang et al., 2005; Jee et al., 2006), as well as for electrical connectors (Harrison and Hodgson, 1976). They indeed provide joints of the greatest mechanical and electrical reliability and integrity, which can be quickly applied or removed. Recently, an experimental and numerical study has been carried out to assess the use of SMA rings as pipe couplers in radioactive areas of high-energy particle accelerators, where thermally induced mounting and dismounting operations can be operated remotely (Niccoli et al., 2017).

In order to exploit the full potential of SMA coupling systems, it becomes essential to estimate the stress distribution within these components accurately. Severe stresses may develop during the production stage or the installation of SMA coupling and may cause unexpected mechanical deformation, damage and failure or just loss of efficiency (Tabesh et al., 2013, 2017). To avoid such technological problems, it becomes necessary to predict the mechanical stresses originated in SMA connections during each step of their production and installation. A complete and detailed understanding of their stress and deformation history will be also useful for improving their design, production and usage conditions.

SMA pipe couplings displaying cylindrical geometries are usually predeformed, so that they must be stored and transported at low temperature and then installed by induction heating (Brook, 1983). They are previously expanded by applying an internal pressure at temperature T_0 over the start Martensite temperature M_s, thus inducing the martensitic transformation. After the coupling is mounted on the pipe the temperature is increased to recover the residual deformation, taking advantage of the reversal austenitic transformation. As a consequence, the coupling diameter decreases and a contact pressure originates between pipe and coupling. In the alternative method proposed by Jee et al. (2006), SMA coupling and pipe are deformed simultaneously and then the coupling is contracted on heating in order to get the tightness also with a poor shape memory effect.

The problem of a SMA ring used as a pipe connector was initially investigated by Brinson and Lammering (1993) by introducing the simplifying assumption of purely elastic behavior along the radial direction. Later, Birman (1999) considered an infinite SMA plate with a circular hole and obtained a closed form approximate solution by assuming a constant ratio between the radial and tan-

E-mail addresses: enrico.radi@unimore.it, eradi@unimore.it

https://doi.org/10.1016/j.ijsolstr.2018.06.034
0020-7683/

gential stresses. Chi et al., (2003, 2005) provided a detailed examination of the axisymmetric stress, strain and phase fraction fields in an annular SMA plate. These analyses were restricted to isothermal loadings and assumed single variant Martensite, so that no unloading process nor reverse transformation to Austenite or negative variant Martensite were taken into consideration. Moreover, the assumption of an effective stress of von Mises type made in those papers necessarily required a numerical approach. In a further paper (Chi et al., 2007), the same authors proposed numerical algorithms for treating cyclic loading histories and applied them to investigate the loading and unloading process of a SMA annular plate.

The study of the process of constrained recovery has been initially limited to uniaxial examples (Liang and Rogers, 1990; Brinson, 1993; Leclercq and Lexcellent, 1996; Kosel and Videnic, 2007). Nagaya and Hirata (1992) developed a simplified model of constrained recovery in SMA rings that considers only the tangential stress and neglects the contribution of radial stresses to the effective stress. Such an extreme simplification allowed these authors to use a uniaxial constitutive model, though it is reasonably accurate only for thin-walled SMA rings. Wang et al. (2005) investigated experimentally the effects of the wall thickness and temperature range on the reverse transformation behavior of SMA pipe joints. Videnic et al. (2008) presented a mathematical model of biaxial constrained recovery in a SMA ring. These authors adopted a generalized effective stress of Tresca type, which allows to consider unequal response in tension and compression. For the sake of simplicity, they assumed a vanishing stress state in the deformed ring after unloading. Such a supposition is not properly correct, since residual stresses are always present in the SMA material after loading-unloading cycle. Piotrowski et al. (2012) performed a combined experimental and finite element analysis of a SMA pipe coupler mounted on an instrumented elastic ring. The coupling pressure predicted by FEA was in excellent agreement with the measured contact pressure. Mirzaeifar et al. (2012) performed a semi-analytic study of the pseudoelastic response of a thick-walled SMA cylinder subject to internal pressure, under plane stress or plane strain conditions. These authors partitioned the cylinder into a finite number of annular regions and provided closed-form solutions for the equilibrium equations in each annulus. Then, a numerical solution was found by solving the system of nonlinear algebraic equations obtained by enforcing stress continuity at the interface between annular regions. Tabesh et al. (2013) provided a closed form solution for the pseudoelastic response of a SMA thick-walled cylinder subjected to internal pressure under plane stress or plane strain loading conditions, for temperature higher than the finish austenitic transformation A_f. They assumed a simplified 2D constitutive model for SMA that incorporates the Tresca transformation criterion with associative flow rule and linear transformation law. Moreover, they considered the simplifying assumption that the axial strain is constant within the wall thickness and thus the response in the axial direction remains elastic. Liu et al. (2013) also performed a similar investigation by considering the effects of a radial temperature gradient. Later, Liu and Du (2014) provided the analytical solution to the problem of isothermal loading of a pseudoelastic SMA cylinder under external pressure. In these analyses the tangential stress is assumed to be always positive, as indeed it occurs during loading and pseudoelastic unloading if the wall thickness is sufficiently thin. In this case the effective Tresca stress is given by the difference between radial and tangential stresses and, thus, the Martensite transformation occurs with elongation in the circumferential direction. However, the results of these investigations show that the tangential stress at the inner radius decreases during the loading process, especially for very large wall thickness. If it becomes null, then a corner of the Tresca transformation condition is attained and transformed Martensite starts elongating along the axial direction also, according to the corner flow rule. Namely, two different Martensite variants are produced within the corner region according to the corner flow rule by means of two different lattice shearing mechanisms, which may develop within the planes orthogonal either to the axial direction or to the tangential direction. Therefore, the latter analyses provide correct predictions for sufficiently thin-walled cylinders, but they may be inaccurate for a very thick-walled SMA cylinder under plane stress loading conditions. In this case, a corner region with null tangential stress may take place during the loading process starting from the inner boundary, as it occurs for an elastic-plastic thick-walled cylinder when the Tresca yield condition is adopted (Koiter, 1953; Durban and Kubi, 1992; Masri and Durban, 2007).

A complete and detailed analytical study of the shape memory effect induced by forward transformations of a very thick SMA cylindrical joint has never been performed by using a constitutive model that incorporates the phase fractions of multiple Martensite variants as internal variables, whose transformation occurs in agreement with the normality rule on the Tresca surface. Most of the simulation available in the literature are commonly performed by using finite element analysis incorporating 3D constitutive models for the thermomechanical behavior of SMAs (Popov and Lagoudas, 2007; Piotrowski et al., 2012, Lagoudas et al., 2012; Zaki, 2012, Niccoli et al., 2017). The purpose of the present study is to develop a rigorous analytical model with closed-form solutions to predict the stress and displacement fields in a SMA ring or thick-walled cylinder composed of several phases, namely Austenite and two different Martensitic variants, subject to internal pressure at constant temperature over the start temperature of the martensitic transformation M_s. In particular, the forward martensitic transformation occurring under proportional axisymmetric loading and plane stress conditions is investigated systematically. The phenomenological SMA constitutive model adopted here assumes that the Martensite fractions evolve as linear functions of the Tresca effective stress, in agreement with the constitutive models proposed by Govindjee and Kasper (1997, 1999), Arghavani et al. (2010), Marfia and Rizzoni (2013) for multi-variants Martensite and by Videnic et al. (2008) and Luig and Bruhns (2008) for single variant Martensite. These models are derived from the theory of generalized plasticity developed by Lubliner and Auricchio (1996) and Auricchio and Lubliner (1997). However, the occurring of the Martensite transformation in SMA according to the corner flow rule of the Tresca criterion has been developed here for the first time, to allow for obtaining closed form solutions to complex 2D or 3D thermomechanical problems. The two Martensite variants consist in the deformed Martensite shortened in the radial direction and stretched in the circumferential or the axial direction, respectively. The activation of one or the other mechanism depends on the stress state according to the normality rule.

Although the general case requires a numerical analysis of two non-linear ODEs, the simplifying assumptions of effective stress in a Tresca form and linear phase transformation kinetic allow us to obtain a closed form solution, also for the regions that are fully transformed to both Martensite variants. Obtaining an analytical solution for these regions is one of the main challenges of the present study. It requires to take into account for the history of loading and the evolution of the volume fractions of Martensite variants within these regions. Despite the theoretical difficulties, analytic solutions have a number of advantages. From them one can see clearly the role played by constitutive and geometrical parameters and thus they allow understanding also more complex problems. Moreover, they provide a reliable evaluation of the residual stresses and strains in the SMA thick-walled cylinder after the isothermal loading process, which can be used also for validating the results of numerical procedures (Auricchio et al., 2014; Bernardini and Pence, 2016).

Please cite this article as: E. Radi, Evolution of multiple Martensite variants in a SMA thick-walled cylinder loaded by internal pressure, International Journal of Solids and Structures (2018), https://doi.org/10.1016/j.ijsolstr.2018.06.034

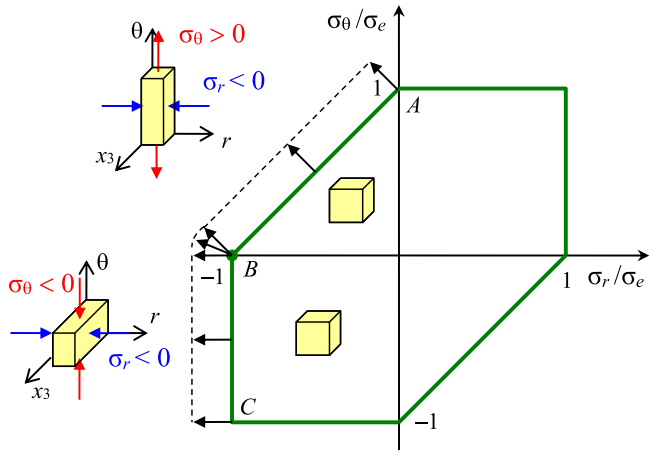

Fig. 1. Tresca transformation condition with associative flow rule and corner flow under plane stress loading conditions ($\sigma_3 = 0$).

The present article is divided into six sections. The constitutive model in the integrated form is briefly reviewed in Section 2. The model is able to describe several phenomena occurring in the radial expansion of a SMA thick-walled cylinder, such as phase transformations, Martensite reorientation and multiple lattice shearing mechanisms. It keeps the essence of the approach used in Videnic et al. (2008) and Tabesh et al. (2013), but extends these studies by considering corner transformation flow rule, thus allowing for the formation of multi-variant Martensite. Moreover, in the present analysis the axial strain may vary within the wall thickness. The general expressions of the stresses, radial displacement and Martensite fraction within all the admissible annular regions that may arise within the cylinder during the loading process, composed of Austenite, Martensite variants and a mixture of such phases, are presented in detail in Section 3. A closed-form solution for the loading process is developed in Section 4 for each possible phase partitioning within the wall thickness and for any value of internal pressure. The solution is obtained by enforcing full stress and displacement continuity at the interface between annular regions and imposing the boundary conditions at the outer and inner radius of the cylinder. Results are presented in Section 5, where the effects of the wall thickness and material parameters on the radial distribution of stresses, radial displacement and Martensite volume fractions are also discussed. A summary of important results is given in Section 6.

2. SMA constitutive model

The equilibrium condition for the in-plane stresses σ_r and σ_θ, which originate in the cylinder under axisymmetric loading conditions, writes

$$\sigma_\theta = r\,\sigma_r' + \sigma_r, \tag{2.1}$$

where the apex denotes the derivative with respect to the variable r. In addition, the strain- displacement compatibility conditions require

$$\varepsilon_r = u_r', \qquad \varepsilon_\theta = \frac{u_r}{r}. \tag{2.2}$$

The phase transformation between Austenite and Martensite is assumed to be governed by the effective stress σ_e given by the Tresca's criterion under plane stress conditions ($\sigma_{33} = 0$). Assuming that the radial stress is always compressive ($\sigma_r < 0$) and $\sigma_r \le \sigma_\theta$, then Tresca's criterion (Fig. 1) gives

$$\sigma_e = \sigma_\theta - \sigma_r, \quad \text{for } \sigma_r \le 0 \le \sigma_\theta, \tag{2.3}$$

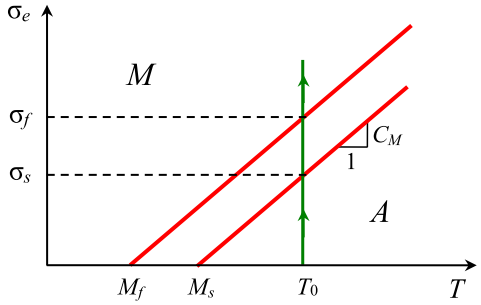

Fig. 2. SMA phase diagram for an isothermal loading process.

$$\sigma_e = -\sigma_r, \quad \text{for } \sigma_r \le \sigma_\theta \le 0. \tag{2.4}$$

Two different Martensite variants may originate during the loading process according to the sign of the tangential stresses σ_θ, as predicted by the Tresca-like transformation condition (2.3) and (2.4) together with the associative flow rule (Fig. 1). The principal Martensite variant is produced for $\sigma_\theta \ge 0$ (side AB in Fig. 1). It causes shortening in the radial direction, elongation in the tangential direction and has no effect on the axial direction. The secondary Martensite variant is produced for $\sigma_\theta \le 0$ (side BC in Fig. 1). It causes shortening in the radial direction, elongation in the axial direction and has no effect on the tangential direction. The volume fractions of these Martensite variants are denoted by $\xi_{r\theta}$ and ξ_{r3}, respectively. Then, the total volume fractions of Martensite is given by the sum $\xi_{tot} = \xi_{r\theta} + \xi_{r3}$.

The threshold stresses σ_s and σ_f for the start and finish martensitic transformations are determined by the temperature T_0 according to the simplified phase diagram sketched in Fig. 2, namely

$$\sigma_s = C_M\,(T_0 - M_s), \quad \sigma_f = C_M\,\left(T_0 - M_f\right), \tag{2.5}$$

being C_M the slope of the martensitic transformation lines.

Although the elastic modulus of the SMA varies during the phase transformation between the elastic modulus E_A of the austenitic phase and the elastic modulus E_M of the martensitic phase, for the sake of simplicity, in the following a constant elastic modulus E is considered for the two phases, equal to the mean value between the two elastic moduli. Moreover, the associative flow rule with corner flow is assumed for the transformation strain, according to the experimental observations of Chirani et al. (2003). Then, the constitutive relations holding for the isothermal and proportional loading process of the *SMA* cylinder under plane stress conditions are assumed in the integrated form (Govindjee and Kasper, 1997, 1999; Videnic et al., 2008; Luig and Bruhns 2008)

$$\begin{aligned}
\varepsilon_r &= \frac{1}{E}(\sigma_r - \nu\sigma_\theta) - \varepsilon_L\,(\xi_{r\theta} + \xi_{r3}),\\
\varepsilon_\theta &= \frac{1}{E}(\sigma_\theta - \nu\sigma_r) + \varepsilon_L\,\xi_{r\theta}, \qquad \text{for } \sigma_r \le 0 \text{ and } \sigma_r < \sigma_\theta\\
\varepsilon_3 &= -\frac{\nu}{E}(\sigma_\theta + \sigma_r) + \varepsilon_L\,\xi_{r3}.
\end{aligned} \tag{2.6}$$

where ε_L is the maximum residual strain obtained by detwinning multiple variant Martensite, coinciding with the maximum inelastic strain attained under uniaxial loading when the solid is composed of fully oriented Martensite. Note from Eq. (2.6) that the martensitic transformation induces no volume change, being of shearing type.

Eqs. (2.6) can be derived by integration of the rate constitutive equations and thus hold for proportional loading. A similar derivation has been performed by Panoskaltsis et al. (2004) for a SMA constitutive model based on an effective stress of von Mises type.

Please cite this article as: E. Radi, Evolution of multiple Martensite variants in a SMA thick-walled cylinder loaded by internal pressure, International Journal of Solids and Structures (2018), https://doi.org/10.1016/j.ijsolstr.2018.06.034

Table 1
Constitutive parameters for SMA materials BL and TA.

	BL	TA
T_0 [°K]	298	340
E [GPa]	46.65	85
ν	0.33	0.4
σ_s [MPa]	153	1200
σ_f [MPa]	223	1400
ε_L	0.067	0.033

Eqs. (2.6) hold also for $\sigma_\theta = 0$, namely when the stress state lays in the corner of the Tresca transformation condition. In this case, the transformation strain is not uniquely defined, in agreement with the corner flow theory of elastic- plastic materials (Durban and Kubi, 1992).

In the following, two different sets of constitutive parameters will be considered. They correspond to those adopted by Brinson and Lammering (1993) and Tabesh et al. (2013) and are denoted by BL and TA, respectively. In particular, the temperature T_0, the Young's modulus E and Poisson coefficient ν of both phases (Martensite and Austenite), the threshold stresses σ_s and σ_f for start and finish martensitic transformations at temperature T_0, and the maximum residual strain ε_L are reported in Table 1 for both sets. For the sake of simplicity, the same values of the Young's modulus and Poisson coefficient are chosen for both phases.

2.1. Martensitic transformation during the loading process

Assuming that the material at the beginning of the loading process is fully austenitic, then, Austenite is transformed into Martensite variants during the loading process. According to the model proposed by Govindjee and Kasper, (1997, 1999), the transformation of the variant Martensite fractions can be expressed in the following integrated form that holds for $\sigma_s \le \sigma_e \le \sigma_f$, with reference to the phase transformation model sketched in Figs. 1 and 2:

$$\xi_{r\theta} = \frac{\sigma_e - \sigma_s}{\sigma_f - \sigma_s}, \quad \xi_{r3} = 0, \ \text{for } \sigma_r < 0 < \sigma_\theta \ \text{and} \ \sigma_e = \sigma_\theta - \sigma_r, \tag{2.7}$$

$$\xi_{r\theta} + \xi_{r3} = \frac{\sigma_e - \sigma_s}{\sigma_f - \sigma_s}, \ \text{for } \sigma_r < \sigma_\theta = 0 \ \text{and} \ \sigma_e = -\sigma_r, \tag{2.8}$$

$$\xi_{r3} = \frac{\sigma_e - \sigma_s}{\sigma_f - \sigma_s} - \xi^0_{r\theta}, \ \xi_{r\theta} = \xi^0_{r\theta}, \ \text{for } \sigma_r < \sigma_\theta < 0 \ \text{and} \ \sigma_e = -\sigma_r, \tag{2.9}$$

where $\xi^0_{r\theta}$ is the principal Martensite variant at the beginning of the transformation.

The dependence of the threshold stresses on the Martensite fraction as depicted in Govindjee and Kasper (1997, 1999) has been neglected here for the sake of conciseness, but it can be easily considered in a more refined investigation, as well as the difference between the elastic moduli of Austenite and Martensite.

2.2. Continuity conditions

Continuity of the radial stress and displacement between two adjacent annular regions undergoing different process of phase transformation must be required. Then, by using $(2.2)_2$ through the front of separation between two different regions one must require

$$[\sigma_r] = [u_r] = [\varepsilon_\theta] = 0, \tag{2.10}$$

where the brackets denote the jump of the function within the brackets. Then from the definition of the effective stress (2.3) and (2.4) and conditions (2.10) it follows

$$[\sigma_e] = \begin{cases} [\sigma_\theta] & \text{for } \sigma_r < 0 < \sigma_\theta \\ 0 & \text{for } \sigma_r < \sigma_\theta \le 0. \end{cases} \tag{2.11}$$

The introduction of (2.10) and (2.11) in the constitutive relations $(2.6)_2$, (2.7) and (2.8), implies

$$[\sigma_\theta] + E\varepsilon_L\,[\xi_{r\theta}] = 0,$$
$$[\sigma_e] = \begin{cases} [\xi_{r\theta}](\sigma_f - \sigma_s) & \text{for } \sigma_r < 0 < \sigma_\theta \\ [\xi_{r\theta} + \xi_{r3}](\sigma_f - \sigma_s) & \text{for } \sigma_r < \sigma_\theta = 0. \end{cases} \tag{2.12}$$

If $\sigma_\theta > 0$ then $\xi_{r3} = 0$ and thus Eqs. (2.11) and (2.12) imply the continuity of the tangential stress, effective stress and volume fraction of Martensite variants during the loading process, namely

$$[\sigma_\theta] = [\sigma_e] = [\xi_{r\theta}] = [\xi_{r3}] = 0, \tag{2.13}$$

whereas if $\sigma_\theta = 0$ then Eqs. (2.11) and (2.12) imply conditions (2.13) and also $[\xi_{r3}] = 0$.

Therefore, continuity of the radial stress and displacement (2.10) also implies continuity of the tangential stress, effective stress and both Martensite volume fractions. In the following, continuity of the radial and effective stresses will be imposed between contiguous annular regions, rather than continuity of the radial displacement.

3. Admissible annular regions within the SMA cylinder

Let r_i and r_o denote the inner and outer radii of the cylinder wall, respectively. Initially the cylinder is everywhere in a state of Austenite, at temperature T_0 higher than the start temperature of the martensitic transformation M_s (Fig. 2). A uniform pressure p is applied at r_i and gradually increased at constant temperature T_0. Correspondingly, the effective stress σ_e is a decreasing function of the radius r whose maximum is attained at r_i. Therefore, the martensitic transformation starts therein when the effective stress reaches the threshold stress σ_s. As the internal pressure is increased, a progressive increase in the volume fraction $\xi_{r\theta}$ of Martensite occurs, starting from r_i. Correspondingly, the front of the start of the Martensite transformation, defined by the radius r_s, moves towards the outer boundary. When the effective stress reaches the threshold stress σ_f at r_i, then a second front corresponding to the finish of the martensitic transformation originates therein. If the internal pressure is further increased, then the second front propagates within the wall thickness with radius r_f.

During the axisymmetric expansion, the wall thickness can be partitioned into three main kinds of annular regions: a purely austenitic outer region A whose inner and outer radii are r_s and r_o, respectively; an intermediate transforming region in a mixture of Austenite and Martensite variants with inner radius r_f and outer radius r_s; and a purely martensitic inner region M with inner radius r_i and outer radius r_f. The intermediate transforming region may be divided in correspondence of the radius r_c into an outer AM region where only the principal Martensite variant $\xi_{r\theta}$ is produced and an inner corner region C where both Martensite variants $\xi_{r\theta}$ and ξ_{r3} are produced. If no corner region takes place within the wall thickness, then, the martensitic inner region M contains the principal variant $\xi_{r\theta}$ alone. If a corner region has instead developed, then the martensitic inner region M^* contains a mixture of both Martensite variants. The number of annular regions within the wall thickness depends on its geometry and internal pressure.

In the following, the general expressions of the stress and displacement fields in the admissible annular regions that take place during each step of the isothermal loading process, are obtained in terms of the internal pressure p and radii r_s, r_c and r_f separating the different annular regions.

Please cite this article as: E. Radi, Evolution of multiple Martensite variants in a SMA thick-walled cylinder loaded by internal pressure, International Journal of Solids and Structures (2018), https://doi.org/10.1016/j.ijsolstr.2018.06.034

3.1. Fully austenitic outer region A

The austenitic region A occupies the outer part of the *SMA* cylinder wall where the martensitic transformation has not started yet, being $\sigma_e < \sigma_s$. Therefore, the SMA within this annular region behaves elastically, being $\xi_{r\theta} = \xi_{r3} = 0$, and the stress field within the austenitic region induced by the tractions $\sigma_r(r_s) = -q_s\ \sigma_s$ exchanged through the front of start martensitic transformation at r_s is predicted by the classical Lamé solution of two-dimensional linear elasticity:

$$\frac{\sigma_r^A(r)}{\sigma_s} = \frac{r_s^2}{r_o^2 - r_s^2}\left(1 - \frac{r_o^2}{r^2}\right) q_s, \tag{3.1}$$

$$\frac{\sigma_\theta^A(r)}{\sigma_s} = \frac{r_s^2}{r_o^2 - r_{Ms}^2}\left(1 + \frac{r_o^2}{r^2}\right) q_s. \tag{3.2}$$

By using Eqs. (3.1) and (3.2) and noting that $\sigma_\theta > \sigma_r$, the effective stress (2.3) in the cylinder wall turns out to be:

$$\frac{\sigma_e^A(r)}{\sigma_s} = \frac{2\ r_s^2}{r_o^2 - r_s^2}\ \frac{r_o^2}{r^2} q_s. \tag{3.3}$$

Under plane stress loading conditions, the radial displacement writes

$$\frac{u_r^A(r)}{r} = \frac{1-\nu}{E}\ \frac{r_s^2}{r_o^2 - r_s^2}\left(1 + \frac{1+\nu}{1-\nu}\ \frac{r_o^2}{r^2}\right) q_s \sigma_s. \tag{3.4}$$

Eqs. (3.1)-(3.4) hold for $r_s \le r \le r_o$.

3.2. Intermediate region AM in a mixture of austenite and principal Martensite variant

Within the region *AM* undergoing phase transformation to the principal Martensite variant, the volume fraction $\xi_{r\theta}$ increases linearly with the effective stress according to relations (2.7). A substitution of Eqs. (2.1) and (2.3) in the constitutive relations (2.6), by using the strain-displacement relations (2.2) and the integrated form of the transformation laws (2.7) to the principal Martensite variant, yields:

$$u_r' = \frac{1}{E}\left[(1-\nu)\ \sigma_r - \left(\nu + \frac{\delta}{1-\delta}\right) r\ \sigma_r' + \frac{\delta}{1-\delta}\ \sigma_s\right], \tag{3.5}$$

$$\frac{u_r}{r} = \frac{1}{E}\left[(1-\nu)\ \sigma_r + \frac{r\ \sigma_r'}{1-\delta} - \frac{\delta}{1-\delta}\ \sigma_s\right], \tag{3.6}$$

where:

$$\delta = \frac{E\varepsilon_L}{\sigma_f - \sigma_s + E\varepsilon_L} < 1, \tag{3.7}$$

is a non-dimensional parameter close to 1, being $E\,\varepsilon_L \gg \sigma_f - \sigma_s$. The introduction of Eq. (3.6) for u_r in (3.5) provides the following linear ODE for the function $\sigma_r(r)$:

$$r^2\ \sigma_r'' + 3\ r\ \sigma_r' - 2\delta\ \sigma_s = 0. \tag{3.8}$$

The analytic solution of the linear ODE (3.8) for the radial stress in the annular region *AM* in a mixture of Austenite and principal variant Martensite ($\xi_{r3} = 0$) is:

$$\frac{\sigma_r^{AM}(r)}{\sigma_s} = A_2 + A_1\frac{r_o^2}{r^2} - \delta \ln\frac{r_o}{r}, \tag{3.9}$$

where A_1 and A_2 are constants of integration. The introduction of (3.9) in Eqs. (2.1), (2.3) and (3.6) provides the following tangential and effective stresses and the radial displacement

$$\frac{\sigma_\theta^{AM}(r)}{\sigma_s} = A_2 - A_1\frac{r_o^2}{r^2} + \delta\left(1 - \ln\frac{r_o}{r}\right), \tag{3.10}$$

$$\frac{\sigma_e^{AM}(r)}{\sigma_s} = \delta - 2\ A_1\ \frac{r_o^2}{r^2}, \tag{3.11}$$

$$\frac{u_r^{AM}(r)}{r} = \frac{\sigma_s}{E}\left[(1-\nu)\left(A_2 - \delta\ \ln\frac{r_o}{r}\right) - A_1\left(\frac{1+\delta}{1-\delta} + \nu\right)\frac{r_o^2}{r^2}\right], \tag{3.12}$$

in terms of the constants A_1 and A_2. Moreover, from (3.11) and (2.7), the volume fraction of transformed Martensite turns out to be:

$$\xi_{r\theta}^{AM}(r) = -\frac{1-\delta}{\gamma - 1}\left(1 + \frac{2\ A_1}{1-\delta}\ \frac{r_o^2}{r^2}\right), \tag{3.13}$$

where

$$\gamma = \frac{\sigma_f}{\sigma_s}, \tag{3.14}$$

is a non-dimensional material parameter greater than 1.

3.3. Corner region C in a mixture of Austenite and both Martensite variants

If the wall thickness is large enough, then, the tangential stress σ_θ may vanish at r_i during the Martensitic transformation. In this case, an annular corner region C appears starting from r_i, where the stress state lays within a corner of the Tresca transformation condition (Fig. 1), in agreement with the problem of a pressurized elastoplastic tube studied by Durban and Kubi (1992). According to (2.1), vanishing of σ_θ within this region leads to the radial stress

$$\frac{\sigma_r^C(r)}{\sigma_s} = -C\ \frac{r_o}{r}, \tag{3.15}$$

where C is a constant. Then, the constitutive Eqs. (2.6), (2.8) and the strain compatibility Eqs. (2.2) imply

$$\frac{u_r}{r} = \frac{\sigma_s}{E}\left[\nu\ C\ \frac{r_o}{r} + \frac{\delta}{1-\delta}\ (\gamma - 1)\ \xi_{r\theta}\right], \tag{3.16}$$

$$(r\ \xi_{r\theta})' + \xi_{r\theta} + \xi_{r3} + \frac{1-\delta}{\gamma - 1}\ \frac{C\ r_o}{\delta\ r} = 0. \tag{3.17}$$

Considering that $\sigma_e = -\sigma_r$ for $\sigma_\theta = 0$, the transformation law (2.8) for the total Martensitic fraction, namely the sum of $\xi_{r\theta}$ and ξ_{r3}, then yields

$$\xi_{r\theta} + \xi_{r3} = \frac{1}{\gamma - 1}\left(C\frac{r_o}{r} - 1\right), \tag{3.18}$$

Eqs. (3.17) and (3.18) provide the following distribution of the Martensite volume fractions $\xi_{r\theta}$ and ξ_{r3} in the corner region in a mixture of Austenite and both Martensite variants

$$\xi_{r\theta}^C(r) = \frac{1}{\gamma - 1}\left(1 - \frac{C\ r_o}{\delta\ r}\ \ln\frac{r}{r_o} + D\frac{r_o}{r}\right), \tag{3.19}$$

$$\xi_{r3}^C(r) = \frac{1}{\gamma - 1}\left[\left(C - D + \frac{C}{\delta}\ln\frac{r}{r_o}\right)\frac{r_o}{r} - 2\right], \tag{3.20}$$

where D is a constant of integration. The radial displacement then follows from $(3.16)_2$, $(2.2)_2$ and (3.19) as

$$\frac{u_r^C(r)}{r} = \frac{\sigma_s}{E}\left[\frac{\delta}{1-\delta}\left(1 + D\frac{r_o}{r}\right) + C\frac{r_o}{r}\left(\eta - \frac{1}{1-\delta}\ln\frac{r}{r_o}\right)\right]. \tag{3.21}$$

Note that a corner region cannot extend till the outer radius of the cylinder wall because the condition $\sigma_r^C(r_o) = 0$ necessarily implies $C = 0$, so that the stress field should be null therein.

Please cite this article as: E. Radi, Evolution of multiple Martensite variants in a SMA thick-walled cylinder loaded by internal pressure, International Journal of Solids and Structures (2018), https://doi.org/10.1016/j.ijsolstr.2018.06.034

3.4. Fully martensitic inner region M

If the loading process is continued after that the complete transformation to both Martensite variants is achieved at r_i, then a fully martensitic region with $\xi_{r\theta}+\xi_{r3}=1$ appears, starting from r_i. The introduction of Eqs. (2.1) and (2.2) in the constitutive Eqs. (2.6) gives:

$$u_r' = \frac{1}{E}\left[(1-\nu)\,\sigma_r - \nu\, r\,\sigma_r'\right] - \varepsilon_L, \tag{3.22}$$

$$\frac{u_r}{r} = \frac{1}{E}\left[(1-\nu)\,\sigma_r + r\,\sigma_r'\right] + \varepsilon_L\,\xi_{r\theta}. \tag{3.23}$$

where $\xi_{r\theta} \le 1$, Two different situations can be envisaged according to the amount of secondary martensitic variant, namely for $\xi_{r3}=0$ or $\xi_{r3} > 0$.

3.4.1. Fully martensitic region M containing only the principal variant

If no corner region takes place within the cylinder wall then $\xi_{r\theta}=1$ and $\xi_{r3}=0$. In this case, the substitution of Eq. (3.23) for u_r in Eq. (3.22) yields the following linear ODE for the function $\sigma_r(r)$:

$$r^2\,\sigma_r'' + 3r\,\sigma_r' + 2E\,\varepsilon_L = 0. \tag{3.24}$$

The linear ODE (3.24) admits the following solution for σ_r, which holds in the fully martensitic region M containing the principal Martensite variant only:

$$\frac{\sigma_r^M(r)}{\sigma_s} = B_2 + B_1\,\frac{r_o^2}{r^2} + \delta\,\frac{\gamma-1}{1-\delta}\ln\frac{r_o}{r}, \tag{3.25}$$

where B_1 and B_2 are constants of integration, being from (3.7) and (3.14)

$$\frac{E\,\varepsilon_L}{\sigma_s} = \delta\,\frac{\gamma-1}{1-\delta}. \tag{3.26}$$

The corresponding equations for the tangential and effective stresses and radial displacement are derived by substituting Eq. (3.25) in (2.1), (2.3) and (3.23) as:

$$\frac{\sigma_\theta^M(r)}{\sigma_s} = B_2 - B_1\,\frac{r_o^2}{r^2} - \delta\,\frac{\gamma-1}{1-\delta}\left(1-\ln\frac{r_o}{r}\right), \tag{3.27}$$

$$\frac{\sigma_e^M(r)}{\sigma_s} = -2\,B_1\,\frac{r_o^2}{r^2} - \delta\,\frac{\gamma-1}{1-\delta}, \tag{3.28}$$

$$\frac{u_r^M(r)}{r} = \frac{\sigma_s}{E}\left[(1-\nu)\left(B_2 + \delta\,\frac{\gamma-1}{1-\delta}\ln\frac{r_o}{r}\right) - B_1(1+\nu)\,\frac{r_o^2}{r^2}\right], \tag{3.29}$$

which hold for $r_i \le r \le r_f$.

3.4.2. Fully martensitic region M* containing both variants

If a corner region C takes place within the cylinder wall, then, both Martensite variants originates therein due to corner flow. In this case, the inner martensitic region M^* is formed by both variants, namely $\xi_{r\theta}+\xi_{r3}=1$. The substitution of Eq. (3.23) for u_r in Eq. (3.22) then yields the following linear ODE for the function $\sigma_r(r)$:

$$r^2\,\sigma_r'' + 3r\,\sigma_r' + E\varepsilon_L\left[1+(r\,\xi_{r\theta})'\right] = 0. \tag{3.30}$$

By using (2.1) and (3.26), the general solution for the stress field satisfying the ODE (3.30) is

$$\frac{\sigma_r^M(r)}{\sigma_s} = \frac{\delta(\gamma-1)}{2(1-\delta)}\left[\left(1-\frac{r_f^2}{r^2}\right)\left(\frac{1}{2}+\xi_{r\theta}^M(r_f)\right) + \ln\frac{r_f}{r} + \int_r^{r_f}\left(\frac{1}{t}+\frac{t}{r^2}\right)\xi_{r\theta}^M(t)\,dt\right] - C_1 - \frac{C_2}{r^2}, \tag{3.31}$$

$$\frac{\sigma_\theta^M(r)}{\sigma_s} = -\frac{\delta(\gamma-1)}{2(1-\delta)}\left[1+2\xi_{r\theta}^M(r) - \left(1+\frac{r_f^2}{r^2}\right)\left(\frac{1}{2}+\xi_{r\theta}^M(r_f)\right) - \ln\frac{r_f}{r} - \int_r^{r_f}\left(\frac{1}{t}-\frac{t}{r^2}\right)\xi_{r\theta}^M(t)dt\right] - C_1 + \frac{C_2}{r^2}, \tag{3.32}$$

where the function $\xi_{r\theta}^M(r)$ denotes the radial distribution of the principal Martensite variant within the M^* region. Since no evolution of the Martensite variants is expected within this region, then the function $\xi_{r\theta}^M(r)$ is defined by the volume fraction of the principal Martensite variant already formed at radius r when the front of the finish martensitic transformation r_f was coinciding with r. The corresponding radial displacement in the fully martensitic region M^* follows from the substitution of Eq. (3.31) in (3.23) as:

$$\frac{u_r(r)}{r} = \frac{\sigma_s}{E}\frac{\delta(\gamma-1)}{1-\delta}\left\{-1-\xi_{r\theta}^M(r) + \left[1-\nu+(1+\nu)\,\frac{r_f^2}{r^2}\right]\left(\frac{1}{2}+\xi_{r\theta}^M(r_f)\right) + (1-\nu)\,\ln\frac{r_f}{r} + \int_r^{r_f}\left(\frac{1-\nu}{t}-\frac{1+\nu}{r^2}t\right)\xi_{r\theta}^M(t)\,dt\right\} - \frac{\sigma_s}{E}\left[(1-\nu)C_1 - (1+\nu)\frac{C_2}{r^2}\right]. \tag{3.33}$$

The integration constants C_1 and C_2 as well as the function $\xi_{r\theta}^M(r)$ must be determined by using the boundary conditions and continuity conditions between adjacent annular regions.

4. Axisymmetric loading process

The unknown parameters introduced in the analytical results for the stresses and radial displacement in the various annular regions obtained in the previous section can be calculated by imposing the boundary conditions at r_i and r_o and the continuity conditions between adjacent annular regions. Depending on the cylinder geometry and the internal pressure, eleven types of phase partitioning of the cylinder wall may occur during the loading process, namely (*A*), (*AM,A*), (*C,AM,A*), (*M*,C,AM,A*), (*C,AM*), (*AM*), (*M*,C,AM*), (*M,AM*), (*M,AM,A*), (*M*,M,AM,*) and (*M*). The distribution of the admissible configurations is sketched in Fig. 3 and preliminary plotted in Fig. 4 as function of the ratio r_i/r_o and normalized internal pressure $q=p/\sigma_s$ for both sets of constitutive parameters BL and TA. The stress and displacement distribution within the wall thickness for a fully austenitic (*A*) cylinder wall may be obtained from the classical linear elastic solution (3.1)-(3.4) for $q_s=q$ and $r_s=r_i$. The other ten admissible configurations are systematically examined in Sections 4.1-4.10.

4.1. Thick-walled cylinder composed of two regions (AM, A)

Let us study first the case of a cylinder wall partitioned in an outer austenitic region *A* and an inner region *AM* in a mixture of Austenite and principal variant Martensite, with $0<\xi_{r\theta}<1$ (Fig. 3*a*). Such a phase distribution occurs for relatively small values of the internal pressure that are not large enough to originate a complete martensitic transformation within the wall thickness. The unknown constants for regions *A* and *AM* are A_1, A_2, q_s and the radius r_s of the front separating the two regions. In order to define these unknown parameters, the following conditions can be imposed at r_s and r_i:

$$\sigma_r^{AM}(r_s) = \sigma_r^A(r_s), \quad \sigma_e^A(r_s) = \sigma_s, \quad \sigma_e^{AM}(r_s) = \sigma_s,$$
$$\sigma_r^{AM}(r_i) = -q\,\sigma_s. \tag{4.1}$$

Please cite this article as: E. Radi, Evolution of multiple Martensite variants in a SMA thick-walled cylinder loaded by internal pressure, International Journal of Solids and Structures (2018), https://doi.org/10.1016/j.ijsolstr.2018.06.034

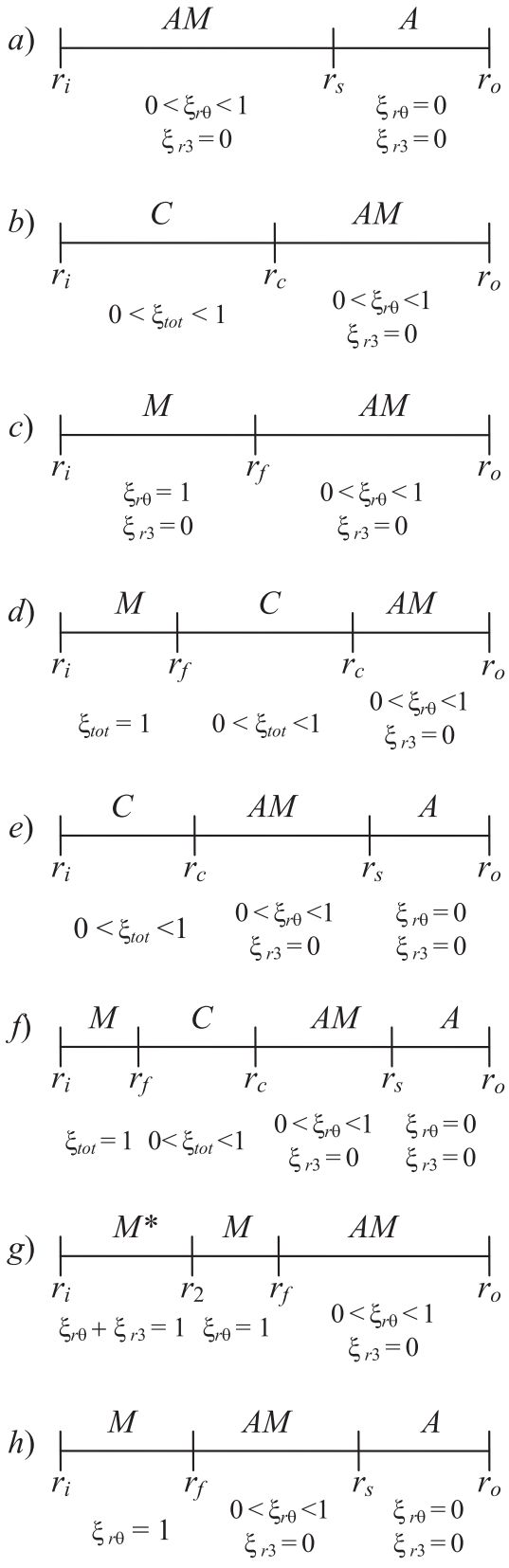

Fig. 3. Sketch of the seven admissible distributions of regions *A*, *AM*, *C*, *M* and *M** within the wall thickness.

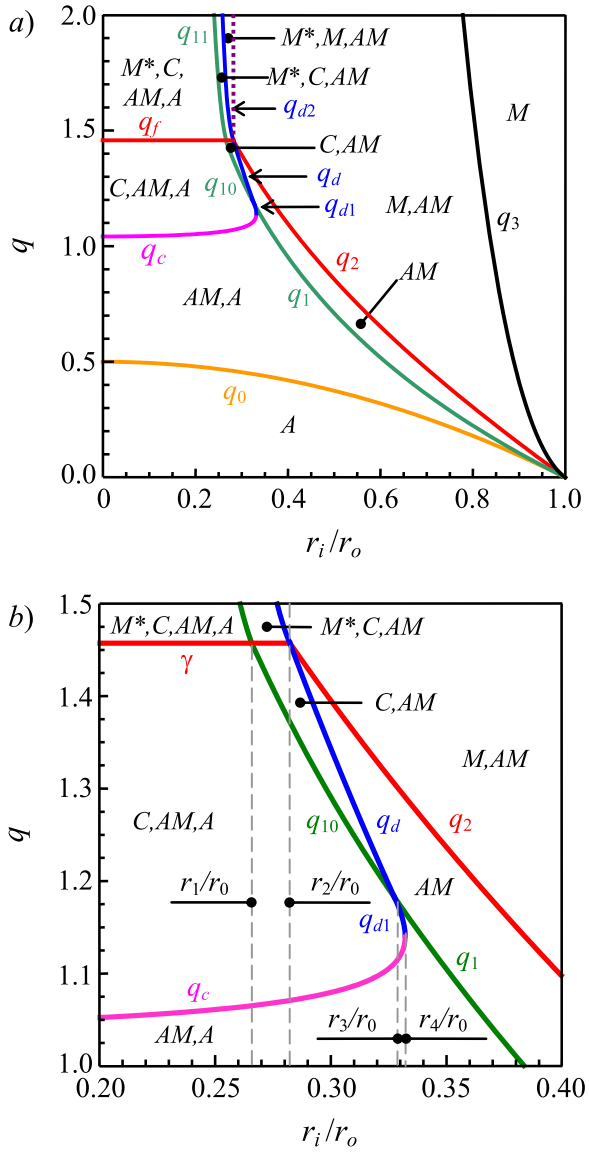

Fig. 4. Variation of the normalized internal pressures separating the admissible phase distributions within the wall thickness with the ratio between inner and outer radii, during the axisymmetric loading process, for SMA material BL (*a*) and corresponding detail (*b*).

As discussed in Section 2.1, continuity of the radial displacement across the interface between two different regions is equivalent to continuity of the effective stress and, thus, it is included within conditions $(4.1)_{2,3}$.

The introduction of (3.3) in condition $(4.1)_2$ provides the following relation between the parameters q_s and r_s

$$q_s = \frac{1}{2}\left(1 - \frac{r_s^2}{r_o^2}\right). \tag{4.2}$$

A substitution of (4.2) in (3.2)-(3.4) thus yields the following stress and displacement fields in the outer austenitic region *A* in terms of r_s

$$\frac{\sigma_r^A(r)}{\sigma_s} = \frac{r_s^2}{2\,r_o^2}\left(1 - \frac{r_o^2}{r^2}\right),$$
$$\frac{\sigma_\theta^A(r)}{\sigma_s} = \frac{r_s^2}{2\,r_o^2}\left(1 + \frac{r_o^2}{r^2}\right),$$

Please cite this article as: E. Radi, Evolution of multiple Martensite variants in a SMA thick-walled cylinder loaded by internal pressure, International Journal of Solids and Structures (2018), https://doi.org/10.1016/j.ijsolstr.2018.06.034

$$\frac{\sigma_e^A(r)}{\sigma_s} = \frac{r_s^2}{r^2},$$
$$\frac{u_r^A(r)}{r} = \frac{\sigma_s}{E}\,\frac{r_s^2}{2\,r_o^2}\left[1-\nu+(1+\nu)\frac{r_o^2}{r^2}\right], \tag{4.3}$$

which hold for $r_s \le r \le r_o$. The introduction of Eqs. (3.2), (3.9) and (3.11) in conditions $(4.1)_{1,3}$ then gives

$$A_1 = -\frac{1-\delta}{2}\,\frac{r_s^2}{r_o^2}, \quad A_2 = \frac{1}{2}\left(\frac{r_s^2}{r_o^2} - \delta - \delta\ln\frac{r_s^2}{r_o^2}\right). \tag{4.4}$$

Therefore, Eqs. (3.9)–(3.13) provide the following stresses, displacement and volume fraction of primary Martensite within the inner region *AM*:

$$\frac{\sigma_r^{AM}(r)}{\sigma_s} = \frac{1}{2}\left[\frac{r_s^2}{r_o^2} - \delta\left(1+\ln\frac{r_s^2}{r^2}\right) - (1-\delta)\,\frac{r_s^2}{r^2}\right],$$
$$\frac{\sigma_\theta^{AM}(r)}{\sigma_s} = \frac{1}{2}\left[\frac{r_s^2}{r_o^2} + \delta\left(1-\ln\frac{r_s^2}{r^2}\right) + (1-\delta)\,\frac{r_s^2}{r^2}\right],$$
$$\frac{\sigma_e^{AM}(r)}{\sigma_s} = \delta + (1-\delta)\,\frac{r_s^2}{r^2},$$
$$\frac{u_r^{AM}(r)}{r} = \frac{\sigma_s}{E}\,\frac{1-\nu}{2}\left[\frac{r_s^2}{r_o^2} + \left(\frac{1+\nu}{1-\nu}+\delta\right)\frac{r_s^2}{r^2} - \delta\left(1+\ln\frac{r_s^2}{r^2}\right)\right],$$
$$\xi_{r\theta}^{AM}(r) = \frac{1-\delta}{\gamma-1}\left(\frac{r_s^2}{r^2}-1\right). \tag{4.5}$$

for $r_i \le r \le r_s$. The introduction of $(4.5)_1$ in the condition $(4.1)_4$ then yields the following relation between the normalized internal pressure q and the radius r_s:

$$q = \frac{1}{2}\left[1-\frac{r_s^2}{r_o^2} + \delta\ln\frac{r_s^2}{r_i^2} - (1-\delta)\left(1-\frac{r_s^2}{r_i^2}\right)\right], \tag{4.6}$$

which hold for $r_i \le r_s \le r_o$. The martensitic transformation starts at r_i when $r_s = r_i$, namely when the normalized pressure (4.6) attains the value

$$q_0 = \frac{1}{2}\left(1-\frac{r_i^2}{r_o^2}\right). \tag{4.7}$$

If the cylinder wall is sufficiently thin, then relation (4.6) holds true until the martensitic transformation starts at r_o while the tangential stress is tensile within the *AM* region. The corresponding internal pressure is $p = q_1\,\sigma_s$, where q_1 is given by (4.6) for $r_s = r_o$, namely

$$q_1 = \frac{1}{2}\left[(1-\delta)\left(\frac{r_o^2}{r_i^2}-1\right) + \delta\ln\frac{r_o^2}{r_i^2}\right]. \tag{4.8}$$

The normalized pressure q_1 separates the wall partitions (*AM*,*A*) and (*AM*) under the further condition $\sigma_\theta^{AM}(r_i) \ge 0$, namely for

$$1+\delta-\delta\,\ln\frac{r_o^2}{r_i^2} + (1-\delta)\frac{r_o^2}{r_i^2} \ge 0, \tag{4.9}$$

according to $(4.5)_2$, or equivalently for $r_i \ge r_3$, where

$$r_3^2 = -\frac{(1-\delta)\,r_o^2}{\delta\,W_0\left(-\frac{1-\delta}{\delta}\,e^{1+1/\delta}\right)}, \tag{4.10}$$

being W_0 the principal branch of the Lambert function (Corless et al., 1996), namely the solution of the equation $W_0(x)\,e^{W_0(x)} = x$, with $W_0(x) \ge -1$ for $x \ge -1/e$.

4.1.1. Complete martensitic transformation along the inner edge of the ring

The complete martensitic transformation is achieved at r_i when the condition $\sigma_e^{AM}(r_i) = \sigma_f$ is met, namely for $r_s = \eta\,r_i$ where

$$\eta = \sqrt{\frac{\gamma-\delta}{1-\delta}} > 1. \tag{4.11}$$

According to (4.6), condition (4.11) is achieved under the internal pressure

$$q_m = \frac{1}{2}\left(\gamma + \delta\ln\eta^2 - \frac{r_i}{r_o}\eta^2\right). \tag{4.12}$$

The result (4.12) holds only if the tangential stress is positive everywhere and the martensitic transformation did not start at r_o yet, namely for $\sigma_\theta^{AM}(r_i) \ge 0$ and $r_s \le r_o$ or equivalently for $r_a \le r_i \le r_b$, where

$$r_a = \frac{r_o}{\eta}\sqrt{\delta\ln\eta^2 - \gamma}, \quad r_b = \frac{r_o}{\eta}. \tag{4.13}$$

Note that for rings whose geometric ratios satisfy $r_o = \eta\,r_i$ the martensitic transformation starts at r_o just when the complete martensitic transformation is achieved at r_i.

4.1.2. Appearing of a corner region C at r_i

If the cylinder wall is thick enough, however, the tangential stress $(4.5)_2$ may vanish at r_i. In this case, the corner region *C* appears at r_i before the martensitic transformation starts at r_o. This condition occurs for $\sigma_\theta^{AM}(r_i) = 0$, namely for

$$\delta\ln\frac{r_s^2}{r_i^2} - (1-\delta)\frac{r_s^2}{r_i^2} = \delta + \frac{r_s^2}{r_o^2}, \tag{4.14}$$

or equivalently

$$\frac{r_s^2}{r_o^2} = -\frac{\delta\,r_i^2}{(1-\delta)\,r_o^2 + r_i^2}\,W_0\left(-\frac{(1-\delta)\,r_o^2 + r_i^2}{\delta\,r_o^2}e\right). \tag{4.15}$$

According to (4.6), the corresponding normalized pressure is then

$$q_c = \delta - \frac{(1-\delta)\,\delta\,r_o^2}{(1-\delta)\,r_o^2 + r_i^2}\,W_0\left(-\frac{(1-\delta)\,r_o^2 + r_i^2}{\delta\,r_o^2}e\right). \tag{4.16}$$

The corner region *C* may disappear for $r_3 < r_i < r_4$, where r_3 is given by (4.10) and

$$r_4^2 = \left(\delta - 1 + \frac{\delta}{e^2}\right)r_o^2, \tag{4.17}$$

when the normalized pressure reaches the value

$$q_{d1} = \delta - \frac{(1-\delta)\,\delta\,r_o^2}{(1-\delta)r_o^2 + r_i^2}\,W_{-1}\left(-\frac{(1-\delta)\,r_o^2 + r_i^2}{\delta\,r_o^2}e\right), \tag{4.18}$$

where W_{-1} is the secondary branch of the Lambert function, namely the solution of the equation $W_{-1}(x)\,e^{W_{-1}(x)} = x$, with $W_{-1}(x) < -1$ for $x \ge -1/e$. Indeed, condition (4.14) is satisfied both for the internal pressures q_c and q_{d1}, where $q_c < q_{d1}$, so that under both pressures the *AM* region extends till the inner radius r_i. Therefore, the cylinder wall is formed by an inner region *AM* in a mixture of phases and an outer austenitic region *A* both for $q_0 < q < \min\{q_1, q_c\}$ and also for $q_{d1} < q < q_1$ if $r_3 < r < r_4$ (see Figs. 4 and 5).

4.2. Thick-walled cylinder composed of three regions (M, AM, A)

For thick rings obeying the condition $r_o > \mathrm{h}\,r_i$ a fully martensitic region appears at r_i for $q = q_m$ before the outer Austenitic region has disappeared (Fig. 3*h*), where q_m has been defined in (4.12). The fields (4.3) and (4.5) defined in terms of r_s hold true in the outer austenitic region *A* where $r_s < r < r_o$, and in the intermediate region *AM* where $r_f < r < r_s$, respectively. According to $(4.5)_3$, the achievement of the condition $\sigma_e^{AM}(r_f) = \sigma_f$ occurs for

$$r_s = \eta\,r_f. \tag{4.19}$$

Therefore, by using (4.19) the stress and displacement fields (4.3) and (4.5) in regions *A* and *AM* can be written in terms of

Please cite this article as: E. Radi, Evolution of multiple Martensite variants in a SMA thick-walled cylinder loaded by internal pressure, International Journal of Solids and Structures (2018), https://doi.org/10.1016/j.ijsolstr.2018.06.034

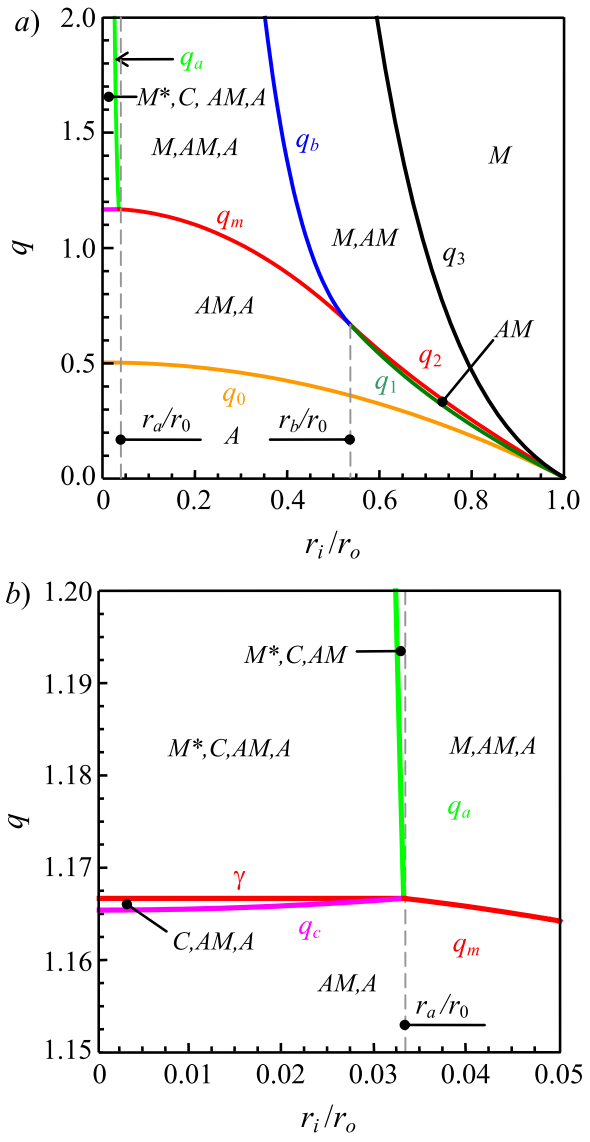

Fig. 5. Variation of the normalized internal pressures separating the admissible phase distributions within the wall thickness with the ratio between inner and outer radii, during the axisymmetric loading process, both for SMA material TA (*a*) and corresponding detail (*b*).

r_f instead of r_s. Then, the radial stress and Martensite volume fraction at the inner radius r_f of the *AM* region follow from Eqs. (4.5)$_{1,5}$ as

$$\frac{\sigma_r^{AM}(r_f)}{\sigma_s} = \frac{1}{2}\left(\frac{r_s^2}{r_o^2} - \gamma - \delta \ln \eta^2\right),$$
$$\frac{\sigma_\theta^{AM}(r_f)}{\sigma_s} = \frac{1}{2}\left(\frac{r_s^2}{r_o^2} + \gamma - \delta \ln \eta^2\right),$$
$$\frac{u_r^{AM}(r_f)}{r} = \frac{\sigma_s}{E}\,\frac{1-\nu}{2}\left(\frac{r_s^2}{r_o^2} + \frac{1+\nu}{1-\nu}\,\eta^2 + \delta\,\eta^2 - \delta \ln \eta^2\right),$$
$$\xi_{r\theta}^{AM}(r_f) = 1. \tag{4.20}$$

By using Eqs. (3.25), (3.27) and (4.20), continuity of the radial and tangential stresses across the interface at r_f, namely $\sigma_r^{AM}(r_f) = \sigma_r^M(r_f)$ and $\sigma_\theta^{AM}(r_f) = \sigma_\theta^M(r_f)$, yields

$$B_1 = -\frac{r_f^2}{2\,r_o^2}\,\eta^2,$$
$$B_2 = \frac{1}{2}\left[\frac{r_f^2}{r_o^2}\,\eta^2 - \delta \ln \eta^2 + \delta\left(\eta^2 - 1\right)\left(1 + \ln \frac{r_f^2}{r_o^2}\right)\right]. \tag{4.21}$$

The introduction of constants B_1 and B_2 in Eqs. (3.25), (3.27)-(3.29) then provides also the distributions of radial stress and displacement within the fully martensitic region *M*, as functions of r_f. Finally, the relation between the normalized internal pressure $q = -\sigma_r^M(r_i)/\sigma_s$ and the radius r_f follows from (3.27) and (4.21) as

$$q = -\frac{1}{2}\left[\eta^2\left(\frac{r_f^2}{r_o^2} - \frac{r_f^2}{r_i^2}\right) + \delta\left(\eta^2 - 1\right)\left(1 + \ln \frac{r_f^2}{r_i^2}\right) - \delta \ln \eta^2\right]. \tag{4.22}$$

4.2.1. Disappearing of the outer austenitic region A

The outer austenitic region *A* disappears from the outer part of the wall thickness when $r_s = r_o$, namely for $r_f = r_o/\eta$ according to (4.19). Then, Eq. (4.22) provides the normalized internal pressure q_b that makes the outer austenitic region *A* disappear

$$q_b = \frac{1}{2}\left(\frac{r_o^2}{r_i^2} - 1\right) + \frac{\delta}{2}\left[\eta^2 \ln \eta^2 - \left(\eta^2 - 1\right)\left(1 + \ln \frac{r_o^2}{r_i^2}\right)\right], \tag{4.23}$$

which holds for $r_i \le r_b$, namely for $\sigma_e^{AM}(r_i) \ge \sigma_f$ according to $(4.5)_3$ for $r_s = r_o$.

4.3. Thick-walled cylinder composed of three regions (C, AM, A)

For thick rings with $r_i < r_4$ a corner region appears at r_i for $q = q_c$ before the outer Austenitic region has disappeared (Fig. 3*e*), where q_c has been defined in (4.16). The fields (4.3) and (4.5) defined in terms of r_s hold true in the outer austenitic region *A*, where $r_s < r < r_o$, and in the intermediate region *AM*, where $r_c < r < r_s$, respectively. The vanishing of the tangential stress at the outer radius of the corner region r_c, namely $\sigma_\theta^{AM}(r_c) = 0$, then yields the following relation between the radii r_s and r_c

$$\delta \ln \frac{r_s^2}{r_c^2} - (1-\delta)\frac{r_s^2}{r_c^2} - \frac{r_s^2}{r_o^2} = \delta, \tag{4.24}$$

or equivalently

$$\frac{r_s^2}{r_c^2} = -\frac{\delta}{1-\delta}\,W_0\left(-\frac{1-\delta}{\delta}\,e^{1+\frac{r_s^2}{\delta\,r_o^2}}\right). \tag{4.25}$$

Correspondingly, the radial stress and Martensite volume fraction at the inner radius of the *AM* region r_c follow from the introduction of (4.24) and (4.25) in Eqs. $(4.5)_{1,5}$ written for $r = r_c$:

$$\frac{\sigma_r^{AM}(r_c)}{\sigma_s} = -(1-\delta)\frac{r_s^2}{r_c^2} - \delta = \delta\left[W_0\left(-\frac{1-\delta}{\delta}\,e^{1+\frac{r_s^2}{\delta\,r_o^2}}\right) - 1\right], \tag{4.26}$$

$$\xi_{r\theta}^{AM}(r_c) = \frac{1-\delta}{\gamma-1}\left(\frac{r_s^2}{r_c^2} - 1\right) = -\frac{1}{\gamma-1}\left[1 - \delta + \delta\,W_0\left(-\frac{1-\delta}{\delta}\,e^{1+r_s^2/(\delta\,r_o^2)}\right)\right]. \tag{4.27}$$

According to (4.25)–(4.26), the corner region *C* appears under the internal pressure q_c defined in (4.16), namely for $r_c = r_i$. By using Eqs. (3.15) and (4.26), continuity of the radial stress across the interface at r_c, namely $\sigma_r^{AM}(r_c) = \sigma_r^C(r_c)$, allows to obtain the constant

$$C = \frac{r_c}{r_o}\left[\delta + (1-\delta)\frac{r_s^2}{r_c^2}\right] = \frac{\delta\,r_c}{r_o}\left[1 - W_0\left(-\frac{1-\delta}{\delta}\,e^{1+\frac{r_s^2}{\delta\,r_o^2}}\right)\right]. \tag{4.28}$$

Please cite this article as: E. Radi, Evolution of multiple Martensite variants in a SMA thick-walled cylinder loaded by internal pressure, International Journal of Solids and Structures (2018), https://doi.org/10.1016/j.ijsolstr.2018.06.034

Then, continuity of the distribution of the principal Martensite across the interface at r_c, namely $\xi^{AM}_{r\theta}(r_c) = \xi^{C}_{r\theta}(r_c)$, by using (3.19), (4.27) and (4.28), yields:

$$D = \frac{r_c}{r_o}\left[\left(\delta + \ln\frac{r_c}{r_o}\right)\left(1 + \frac{1-\delta}{\delta}\frac{r_s^2}{r_c^2}\right) - 2\right] = \frac{r_c}{r_o}\left\{\left(\delta + \ln\frac{r_c}{r_o}\right)\left[1 - W_0\left(-\frac{1-\delta}{\delta}e^{1+r_s^2/(\delta\, r_o^2)}\right)\right] - 2\right\}. \quad (4.29)$$

Note that the condition $\xi^{C}_{r3}(r_c) = 0$ is also met by Eqs. (4.28) and (4.29). The introduction of the constants C and D in Eqs. (3.15), (3.19), (3.20) and (3.21) then provides the distributions of radial stress, displacement and Martensite fractions within the corner region. In particular, from (3.15), (3.21) and (4.28), (4.29) the radial stress and displacement at r_i turn out to be

$$\frac{\sigma_r^C(r_i)}{\sigma_s} = -\frac{r_c}{r_i}\left[\delta + (1-\delta)\frac{r_s^2}{r_c^2}\right] = -\delta\,\frac{r_c}{r_i}\left[1 - W_0\left(-\frac{1-\delta}{\delta}\,e^{1+r_s^2/(\delta\, r_o^2)}\right)\right],$$
$$\frac{u_r^C(r_i)}{r_i} = \frac{\sigma_s}{E}\frac{\delta}{1-\delta}\left[1 - 2\frac{r_c}{r_i} + \frac{r_c}{r_i}\left(1 + \frac{1-\delta}{\delta}\frac{r_s^2}{r_c^2}\right) \times \left(\nu - \delta\nu + \delta + \ln\frac{r_c}{r_i}\right)\right]. \quad (4.30)$$

where r_c is given by (4.25) as a function of r_s. Therefore, the relation between the normalized internal pressure $q = -\sigma_r^C(r_i)/\sigma_s$ and the radius r_s for $q_c \le q \le \gamma$ follows from $(4.30)_1$ and (4.25) as

$$q = \frac{r_s}{r_i}\,\frac{1 - W_0\left(-\frac{1-\delta}{\delta}\,e^{1+r_s^2/(\delta\, r_o^2)}\right)}{\sqrt{-\,W_0\left(-\frac{1-\delta}{\delta}\,e^{1+r_s^2/(\delta\, r_o^2)}\right)}}\,\sqrt{(1-\delta)\,\delta}\,. \quad (4.31)$$

4.3.1. Start of the martensitic transformation at r_o

The outer austenitic region A disappears when $r_s = r_o$, namely from (4.24)

$$\delta\ln\frac{r_o^2}{r_c^2} - (1-\delta)\frac{r_o^2}{r_c^2} = 1 + \delta, \quad (4.32)$$

i.e. for $r_c = r_3$, where r_3 has been defined in (4.10). Then, by using Eq. (4.25) for $r_s = r_o$, from (4.31) one obtains the pressure q_{10} that makes the outer austenitic region A disappear

$$q_{10} = \left[(1-\delta)\frac{r_0^2}{r_3^2} + \delta\right]\frac{r_3}{r_i}. \quad (4.33)$$

Therefore, under the pressure q_{10} the cylinder wall is partitioned into an outer region AM in a mixture of phases and an inner corner region C, as it may be observed in Fig. 4.

4.3.2. Complete martensitic transformation achieved at r_i

The complete Martensitic transformation is attained at r_i when $\sigma_e^C(r_i) = -\sigma_r^C(r_i) = \sigma_f$, namely for $q = \gamma$. The constant C is then given by Eq. (3.15) evaluated at r_i

$$C = \gamma\,\frac{r_i}{r_o}. \quad (4.34)$$

Then, by using (4.30) and definition (3.14), the condition $\sigma_r^C(r_i) = -\gamma\,\sigma_f$ yields the following relation between the radii r_s and r_c

$$r_s^2 = \frac{\delta}{1-\delta}\left(\frac{\gamma}{\delta}\,\frac{r_i}{r_c} - 1\right)r_c^2. \quad (4.35)$$

The constant D follows from (4.29) and (4.35) in terms of r_c as

$$D = \gamma\left(1 + \frac{1}{\delta}\,\ln\frac{r_c}{r_o}\right)\frac{r_i}{r_o} - 2\,\frac{r_c}{r_o}. \quad (4.36)$$

Finally, the size r_c of the corner region can be found by solving the transcendental equation obtained from the introduction of (4.35) in (4.24):

$$\ln\left(\frac{\gamma}{\delta}\,\frac{r_i}{r_c} - 1\right) - \left(\frac{\gamma}{\delta}\,\frac{r_i}{r_c} - 1\right)\left(1 + \frac{1}{1-\delta}\,\frac{r_c^2}{r_o^2}\right) = 1 + \ln\frac{1-\delta}{\delta}. \quad (4.37)$$

Eq (4.37) admits multiple solutions for the radius r_c for the same value of r. However, only the solution satisfying $r_i < r_c < r_4$ must be retained, i.e.:

$$r_i = \begin{cases} \dfrac{\delta}{\gamma}\left[1 - \dfrac{(1-\delta)\,r_o^2}{(1-\delta)\,r_o^2 + r_c^2}\,W_0\left(-\,\dfrac{(1-\delta)\,r_o^2 + r_c^2}{\delta\,r_o^2}\,e\right)\right]r_c, \\ \quad \text{for } r_i \le r_{lim}, \\ \dfrac{\delta}{\gamma}\left[1 - \dfrac{(1-\delta)\,r_o^2}{(1-\delta)\,r_o^2 + r_c^2}\,W_{-1}\left(-\,\dfrac{(1-\delta)\,r_o^2 + r_c^2}{\delta\,r_o^2}\,e\right)\right]r_c, \\ \quad \text{for } r_i > r_{lim} \text{ and } r_3 \le r_c \le r_4. \end{cases} \quad (4.38)$$

where

$$r_{\lim} = \frac{r_o}{e\,\gamma}\left[\delta + (1-\delta)e^2\right]\sqrt{\delta - (1-\delta)e^2}. \quad (4.39)$$

The corresponding stress and displacement fields and the distribution of both Martensite variants within the corner region can be found by introducing in (3.15), (3.19), (3.20) and (3.21) the constants C and D found in (4.34) and (4.36), where the radii r_c is defined by Eq. (4.38). In particular, from Eqs. (3.19) and (3.20) the following volume fractions of both Martensite variants are found at r_i:

$$\xi^C_{r\theta}(r_i) = \frac{1}{\gamma - 1}\left(\gamma + 1 - 2\frac{r_c}{r_i} + \frac{\gamma}{\delta}\,\ln\frac{r_c}{r_i}\right),$$
$$\xi^C_{r3}(r_i) = \frac{1}{\gamma - 1}\left(2\frac{r_c}{r_i} - 2 - \frac{\gamma}{\delta}\,\ln\frac{r_c}{r_i}\right), \quad (4.40)$$

namely where the complete martensitic transformation has been achieved, so that $\xi^C_{r3}(r_i) + \xi^C_{r\theta}(r_i) = 1$.

4.4. Thick-walled cylinder composed of four regions (M, C, AM, A)*

For very thick rings a Martensite region M may appear at r_i while an Austenite region A is still present at r_o (Fig. 3*f*). In this case, Eqs. (4.3) and (4.5) define the radial distributions of the various fields in the outer region A, namely for $r_s < r < r_o$, and in the intermediate region AM, namely for $r_c < r < r_s$. Moreover, Eq. (4.25) provides a relation between the radii r_s and r_c.

In the adjacent corner region C occurring for $r_f < r < r_c$, the fields are defined by means of the constants C and D according to Eqs. (3.15), (3.19)-(3.21). By using Eq. (3.15), the constant C follows from the condition $\sigma_r^C(r_f) = -\sigma_f$ as

$$C = \gamma\,\frac{r_f}{r_o}. \quad (4.41)$$

By replacing the radius r_i with r_f in Eq. (4.38), then, the radius r_c follows as an implicit function of r_f, namely by inverting the following relation

$$r_f = \begin{cases} \dfrac{\delta}{\gamma}\left[1 - \dfrac{(1-\delta)\,r_o^2}{(1-\delta)\,r_o^2 + r_c^2}\,W_0\left(-\,\dfrac{1-\delta+r_c^2/r_o^2}{\delta}\,e\right)\right]r_c, \\ \quad \text{for } r_f \le r_{lim} \text{ and } r_f \le r_c \le r_4, \\ \dfrac{\delta}{\gamma}\left[1 - \dfrac{(1-\delta)\,r_o^2}{(1-\delta)\,r_o^2 + r_c^2}\,W_{-1}\left(-\,\dfrac{1-\delta+r_c^2/r_o^2}{\delta}\,e\right)\right]r_c, \\ \quad \text{for } r_f > r_{lim} \text{ and } r_3 \le r_c \le r_4, \end{cases} \quad (4.42)$$

Please cite this article as: E. Radi, Evolution of multiple Martensite variants in a SMA thick-walled cylinder loaded by internal pressure, International Journal of Solids and Structures (2018), https://doi.org/10.1016/j.ijsolstr.2018.06.034

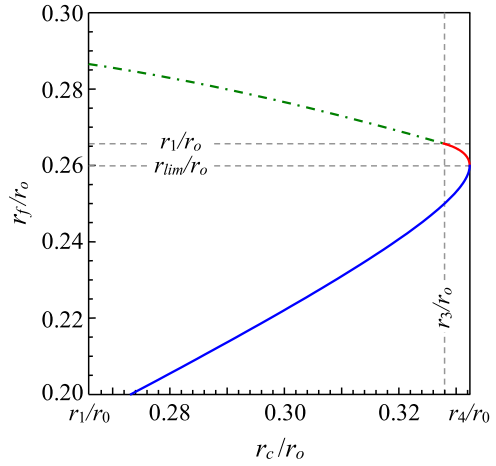

Fig. 6. Relation between r_f and r_c provided by Eq. (4.35) (solid lines) and by Eq. (4.60) (dash-dotted line).

where $r_i \le r_f \le r_1$ and $r_f \le r_c \le r_4$, where the radius r_1 is defined as the radius r_f when r_s coincides with r_o (see Section 4.4.1). The relation between r_f and r_c defined in (4.42) has been plotted in Fig. 6 by solid lines. Then, continuity of the distribution of the principal Martensite volume fraction across the interface at r_c, namely $\xi^{AM}_{r\theta}(r_c) = \xi^{C}_{r\theta}(r_c)$, by using (3.19), (4.27), (4.41) and (4.42), yields:

$$D = \frac{r_c}{r_o}\left[-2 + \frac{\gamma}{\delta}\left(\delta + \ln\frac{r_c}{r_o}\right)\frac{r_f}{r_c}\right]. \tag{4.43}$$

The introduction of the constants C and D in (3.15), (3.19)-(3.21) then provides the following fields within the corner region C in terms of the radii r_c and r_f.

$$\begin{aligned}
\frac{\sigma^C_r(r)}{\sigma_s} &= -\gamma\ \frac{r_f}{r},\\
\xi^C_{r\theta}(r) &= \frac{1}{\gamma-1}\left[1 - 2\frac{r_c}{r} + \frac{\gamma}{\delta}\left(\delta + \ln\frac{r_c}{r}\right)\frac{r_f}{r}\right],\\
\xi^C_{r3}(r) &= \frac{1}{\gamma-1}\left(2\frac{r_c}{r} - 2 - \frac{\gamma}{\delta}\frac{r_f}{r}\ \ln\frac{r_c}{r}\right),\\
\frac{u^C_r(r)}{r} &= \frac{\sigma_s}{E}\frac{\delta}{1-\delta}\left[1 - 2\frac{r_c}{r} + \frac{\gamma}{\delta}\ \left(\delta + \nu - \nu\delta + \ln\frac{r_c}{r}\right)\frac{r_f}{r}\right].
\end{aligned} \tag{4.44}$$

The constants C_1 and C_2 defining the stress and displacement fields (3.31)–(3.33) in the martensitic region M^* surrounded by the corner region C can be calculated by imposing stress continuity between the martensitic region M^* and the adjacent corner region C at r_f, namely $\sigma^M_r(r_f) = -\sigma_f$ and $\sigma^M_\theta(r_f) = 0$. By using (3.31) and (3.32), the latter conditions provide

$$C_1 = \frac{\gamma}{2}, \quad C_2 = \frac{\gamma}{2}\ r_f^2, \tag{4.45}$$

Therefore, the following stress and displacement fields take place in the martensitic region M^*:

$$\begin{aligned}
\frac{\sigma^M_r(r)}{\sigma_s} &= \delta\frac{\eta^2-1}{2}\left[\left(1 - \frac{r_f^2}{r^2}\right)\left(\frac{1}{2} + \xi^M_{r\theta}(r_f)\right)\right.\\
&\quad \left. + \ln\frac{r_f}{r} + \int_r^{r_f}\left(\frac{1}{t} + \frac{t}{r^2}\right)\xi^M_{r\theta}(t)\ dt\right] - \frac{\gamma}{2}\left(1 + \frac{r_f^2}{r^2}\right),\\
\frac{\sigma^M_\theta(r)}{\sigma_s} &= -\delta\frac{\eta^2-1}{2}\left[1 + 2\xi^M_{r\theta}(r) - \left(1 + \frac{r_f^2}{r^2}\right)\left(\frac{1}{2} + \xi^M_{r\theta}(r_f)\right)\right.\\
&\quad \left. - \ln\frac{r_f}{r} - \int_r^{r_f}\left(\frac{1}{t} - \frac{t}{r^2}\right)\xi^M_{r\theta}(t)dt\right] - \frac{\gamma}{2}\left(1 - \frac{r_f^2}{r^2}\right).
\end{aligned}$$

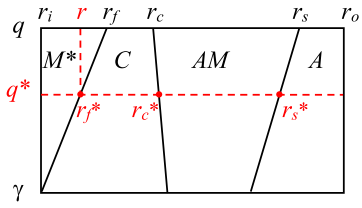

Fig. 7. Sketch and definition of radii r_f^*, r_c^* and r_s^* as functions of r, for $r_i < r < r_f$ for the (M^*,C, AM,A) phase partitioning.

$$\begin{aligned}
\frac{u_r(r)}{r} &= -\frac{\sigma_s}{E}\delta\ \frac{\eta^2-1}{2}\left\{1 + \xi^M_{r\theta}(r) - \left[1 - \nu + (1+\nu)\ \frac{r_f^2}{r^2}\right]\right.\\
&\quad \left(\frac{1}{2} + \xi^M_{r\theta}(r_f)\right) - (1-\nu)\ \ln\frac{r_f}{r}\\
&\quad \left. + \int_{r_f}^{r}\left(\frac{1-\nu}{t} - \frac{1+\nu}{r^2}t\right)\xi^M_{r\theta}(t)\ dt\right\}\\
&\quad - \frac{\sigma_s}{E}\frac{\gamma}{2}\left[1 - \nu - (1+\nu)\frac{r_f^2}{r^2}\right].
\end{aligned} \tag{4.46}$$

namely for $r_i < r < r_f$.

In order to define the distribution of the principal Martensite variant $\xi^M_{r\theta}(r)$ within the region M^*, let us denote with r_c^* the outer radius of the corner region C under the normalized internal pressure q^* acting when the finish martensitic transformation occurred at radius r as sketched in Fig. 7, where $\gamma \le q^* \le q$. Then, the stress and displacement fields within the region M^* follow from Eqs. (4.46) where the function $\xi^M_{r\theta}(r)$ is defined by condition $(4.40)_1$ written for $r_i = r \le r_f$ and $r_c = r_c^*$, namely

$$\xi^M_{r\theta}(r) = 1 - \frac{1}{\gamma-1}\left(2\frac{r_c^*}{r} - 2 - \frac{\gamma}{\delta}\ \ln\frac{r_c^*}{r}\right), \tag{4.47}$$

and r_c^* is defined as an implicit function of r by relation (4.42) written for $r_f = r$ and $r_c = r_c^*$, namely

$$r = \begin{cases}
\dfrac{\delta}{\gamma}\left[1 - \dfrac{(1-\delta)\ r_o^2}{(1-\delta)\ r_o^2 + r_c^{*2}}W_0\left(-\dfrac{(1-\delta)\ r_o^2 + r_c^{*2}}{\delta\ r_o^2}e\right)\right]r_c^*,\\
\text{for } r \le r_{lim} \text{ and } r \le r_c^* \le r_4,\\
\dfrac{\delta}{\gamma}\left[1 - \dfrac{(1-\delta)\ r_o^2}{(1-\delta)\ r_o^2 + r_c^{*2}}W_{-1}\left(-\dfrac{(1-\delta)\ r_o^2 + r_c^{*2}}{\delta\ r_o^2}e\right)\right]r_c^*,\\
\text{for } r > r_{lim} \text{ and } r_3 \le r_c^* \le r_4,
\end{cases} \tag{4.48}$$

for $r_i < r < r_f$. Moreover, by requiring that the radial stress at r_i must coincide with the internal pressure, namely $\sigma^M_r(r_i) = -q\ \sigma_s$, then from $(4.46)_1$ it follows $q = Q(r_f)$, where

$$\begin{aligned}
Q(r) &= -\delta\frac{\eta^2-1}{2}\left[\left(1 - \frac{r^2}{r_i^2}\right)\left(\frac{1}{2} + \xi^M_{r\theta}(r)\right)\right.\\
&\quad \left. + \ln\frac{r}{r_i} + \int_{r_i}^{r}\left(\frac{1}{t} + \frac{t}{r_i^2}\right)\xi^M_{r\theta}(t)\ dt\right] + \frac{\gamma}{2}\left(1 + \frac{r^2}{r_i^2}\right).
\end{aligned} \tag{4.49}$$

The radius r_f thus follows as an implicit function of the normalized internal pressure q. Finally, the radii r_c and r_s follow from relations (4.42) and (4.24), respectively. Note that relation (4.24) can be explicitly solved for r_s as a function of r_c under the restriction $r_c < r_s < r_o$, i.e.

$$r_s^2 = \begin{cases}
-\dfrac{\delta\ r_c^2\ r_o^2}{(1-\delta)\ r_o^2 + r_c^2}\ W_0\left(-\dfrac{(1-\delta)\ r_o^2 + r_c^2}{\delta\ r_o^2}e\right), & \text{for } q \le q_4,\\
-\dfrac{\delta\ r_c^2\ r_o^2}{(1-\delta)\ r_o^2 + r_c^2}\ W_{-1}\left(-\dfrac{(1-\delta)\ r_o^2 + r_c^2}{\delta\ r_o^2}e\right), & \text{for } q > q_4.
\end{cases} \tag{4.50}$$

where

$$q_4 = Q\Big(\big[\delta + (1-\delta)e^2\big]r_4/\gamma\Big), \tag{4.51}$$

is the normalized pressure under which the corner region C attains the maximum extension $r_c = r_4$.

4.4.1. Start of the martensitic transformation at r_o

The outer austenitic region A disappears when $r_s = r_o$, namely for $r_c = r_3$, where r_3 is given by (4.10). Then, from (4.42) for $r_c = r_3$, by using (4.9) one gets $r_f = r_1$, where

$$r_1 = \frac{1}{\gamma}\left[(1-\delta)\frac{r_0^2}{r_3^2} + \delta\right] r_3, \tag{4.52}$$

being $r_{lim} \le r_1 \le r_3$. The normalized pressure q_{11} that makes the outer austenitic region A disappear then follows from the introduction of (4.10) and (4.52) in the condition $q_{11} = Q(r_1)$ and $\xi^M_{r\theta}(r)$ has been defined in (4.47) and (4.48). Moreover, from $(4.40)_1$ one has

$$\xi^M_{r\theta}(r_1) = \xi^C_{r\theta}(r_1) = \frac{1}{\gamma - 1}\left(\gamma + 1 - 2\frac{r_3}{r_1} + \frac{\gamma}{\delta}\ln\frac{r_3}{r_1}\right). \tag{4.53}$$

Under the pressure $q_{11} = Q(r_1)$ the cylinder wall is partitioned into an outer region AM in a mixture of phases an intermediate corner region C and an inner martensitic region M^*

4.4.2. Vanishing of the corner region C

As the internal pressure increases, the corner region C may disappear if the condition $r_c = r_f = r_a$ is attained according to (4.42), where r_a has been defined in (4.13). The corresponding internal pressure q_b that makes the corner region C disappear is then given by

$$q_a = Q(r_a). \tag{4.54}$$

4.5. Thick-walled cylinder composed of two regions (C, AM)

After the corner region C appeared at r_i and the austenitic region A disappeared under the normalized pressure q_{10}, then for slightly higher pressure the cylinder wall is partitioned into an outer region AM in a mixture of phases for $r_c < r < r_o$ and an inner corner region C for $r_i < r < r_c$ (Fig. 3*b*), where the radius r_c is defined by the condition $\sigma^{AM}_\theta(r_c) = 0$. In this case, the conditions $\sigma^{AM}_r(r_o) = 0$ and $\sigma^{AM}_\theta(r_c) = 0$ provide the following constants

$$A_1 = -A_2 = \frac{\delta\, r_c^2}{r_o^2 + r_c^2}\left(1 - \ln\frac{r_o}{r_c}\right), \tag{4.55}$$

which define the fields (3.9)–(3.13) in the outer AM region in terms of the radius r_c. The corresponding stress and displacement fields and the distribution of the volume fraction of the principal Martensite variant within the AM region are given by (3.9)–(3.13) as

$$\begin{aligned}
\frac{\sigma^{AM}_r(r)}{\sigma_s} &= -\frac{\delta\, r_c^2}{r_o^2 + r_c^2}\left(1 - \ln\frac{r_o}{r_c}\right)\left(1 - \frac{r_o^2}{r^2}\right) - \delta\ln\frac{r_o}{r},\\
\frac{\sigma^{AM}_\theta(r)}{\sigma_s} &= -\frac{\delta\, r_c^2}{r_o^2 + r_c^2}\left(1 - \ln\frac{r_o}{r_c}\right)\left(1 + \frac{r_o^2}{r^2}\right) + \delta\left(1 - \ln\frac{r_o}{r}\right),\\
\frac{\sigma^{AM}_e(r)}{\sigma_s} &= \delta\left[1 - \frac{2\, r_c^2}{r_o^2 + r_c^2}\left(1 - \ln\frac{r_o}{r_c}\right)\frac{r_o^2}{r^2}\right],\\
\frac{u^{AM}_r(r)}{r} &= -\frac{\sigma_s}{E}\delta\left\{\frac{r_c^2}{r_o^2 + r_c^2}\left(1 - \ln\frac{r_o}{r_c}\right)\left[1 - \nu + \left(\frac{1+\delta}{1-\delta} + \nu\right)\frac{r_o^2}{r^2}\right]\right.\\
&\quad \left. + (1-\nu)\ln\frac{r_o}{r}\right\},\\
\xi^{AM}_{r\theta}(r) &= -\frac{1}{\gamma - 1}\left[1 - \delta + \frac{2\delta\, r_c^2}{r_o^2 + r_c^2}\left(1 - \ln\frac{r_o}{r_c}\right)\frac{r_o^2}{r^2}\right].
\end{aligned} \tag{4.56}$$

The radial stress and Martensite volume fraction at the inner radius of the AM region r_c are

$$\begin{aligned}
\frac{\sigma^{AM}_r(r_c)}{\sigma_s} &= \frac{\delta\, r_o^2}{r_o^2 + r_c^2}\left(1 - \frac{r_c^2}{r_o^2} + \ln\frac{r_c^2}{r_o^2}\right),\\
\xi^{AM}_{r\theta}(r_c) &= -\frac{1}{\gamma - 1}\left[1 - \delta + \frac{\delta\, r_o^2}{r_o^2 + r_c^2}\left(2 + \ln\frac{r_c^2}{r_o^2}\right)\right],
\end{aligned} \tag{4.57}$$

respectively. As the load is increased, the corner region C takes place for $q \ge q_c$ and $r_i \le r_4$. For $r_3 \le r_i \le r_4$ the corner region then disappears under the normalized pressure

$$q_d = -\frac{\delta\, r_o^2}{r_o^2 + r_i^2}\left(1 - \frac{r_i^2}{r_o^2} + \ln\frac{r_i^2}{r_o^2}\right) \le q_f, \tag{4.58}$$

as it follows from $(4.57)_1$ for $r_c = r_i$. The variation of q_d with the wall thickness is plotted in Fig. 4 and detailed in Fig. 5.

The unknown constants C and D can be obtained in terms of r_c by imposing continuity of the radial stress and volume fraction of the principal Martensite variant across the interface at r_c, namely $\sigma^{AM}_r(r_c) = \sigma^C_r(r_c)$ and $\xi^{AM}_{r\theta}(r_c) = \xi^C_{r\theta}(r_c)$, by using (3.15), (3.19), and (4.57):

$$\begin{aligned}
C &= -\frac{\delta\, r_o^2}{r_o^2 + r_c^2}\left(1 - \frac{r_c^2}{r_o^2} + \ln\frac{r_c^2}{r_o^2}\right)\frac{r_c}{r_o},\\
D &= -\frac{r_c}{r_o}\left[2 + \frac{r_o^2}{r_o^2 + r_c^2}\left(1 - \frac{r_c^2}{r_o^2} + \ln\frac{r_c^2}{r_o^2}\right)\left(\delta + \ln\frac{r_c}{r_o}\right)\right].
\end{aligned} \tag{4.59}$$

Note that these constants C and D also satisfy the continuity condition $\xi^C_{r3}(r_c) = 0$ according to (3.20). Then, the introduction of constants C and D in Eqs. (3.15), (3.19), (3.20) and (3.21) provides the following distributions of radial stress, displacement and Martensite fractions within the corner region

$$\begin{aligned}
\frac{\sigma^C_r(r)}{\sigma_s} &= \frac{\delta\, r_o^2}{r_o^2 + r_c^2}\left(1 - \frac{r_c^2}{r_o^2} + \ln\frac{r_c^2}{r_o^2}\right)\frac{r_c}{r},\\
\frac{u^C_r(r)}{r} &= \frac{\sigma_s}{E}\frac{\delta}{1-\delta}\left[1 - 2\frac{r_c}{r} - \frac{r_o^2}{r_o^2 + r_c^2}\frac{r_c}{r}\left(1 - \frac{r_c^2}{r_o^2} + \ln\frac{r_c^2}{r_o^2}\right)\right.\\
&\quad \left.\left(\nu + \delta(1-\nu) + \ln\frac{r_c}{r}\right)\right].\\
\xi^C_{r\theta}(r) &= \frac{1}{\gamma - 1}\left\{1 - \left[2 + \frac{r_o^2}{r_o^2 + r_c^2}\left(1 - \frac{r_c^2}{r_o^2} + \ln\frac{r_c^2}{r_o^2}\right)\right.\right.\\
&\quad \left.\left.\left(\delta + \ln\frac{r_c}{r}\right)\right]\frac{r_c}{r}\right\},\\
\xi^C_{r3}(r) &= \frac{1}{\gamma - 1}\left\{\left[2 + \frac{r_o^2}{r_o^2 + r_c^2}\left(1 - \frac{r_c^2}{r_o^2} + \ln\frac{r_c^2}{r_o^2}\right)\ln\frac{r_c}{r}\right]\frac{r_c}{r} - 2\right\}.
\end{aligned} \tag{4.60}$$

According to $(4.60)_1$, the following relation holds between the normalized internal pressure q and the outer radius of the corner region r_c

$$q = -\frac{\delta\, r_o^2}{r_o^2 + r_c^2}\left(1 - \frac{r_c^2}{r_o^2} + \ln\frac{r_c^2}{r_o^2}\right)\frac{r_c}{r_i}. \tag{4.61}$$

4.5.1. Complete martensitic transformation achieved at r_i

The complete Martensitic transformation is achieved at r_i for $q = \gamma$. Correspondingly, the radius r_c is defined by the condition $\sigma^C_r(r_i) = -\sigma_f$, namely

$$\left(1 - \frac{r_c^2}{r_o^2} + \ln\frac{r_c^2}{r_o^2}\right)\frac{r_c}{r_i} + \frac{\gamma}{\delta}\left(1 + \frac{r_c^2}{r_o^2}\right) = 0. \tag{4.62}$$

Note that Eq. (4.62) admits two solutions for the radius r_c. However, only the solution satisfying $r_i \le r_c \le r_o$ must be retained, namely the largest. By using (4.62), Eqs. (4.59) provide the same

Please cite this article as: E. Radi, Evolution of multiple Martensite variants in a SMA thick-walled cylinder loaded by internal pressure, International Journal of Solids and Structures (2018), https://doi.org/10.1016/j.ijsolstr.2018.06.034

constants C and D obtained in (4.34) and (4.36) and, thus, the same fields within the corner region found in Section 4.3.2.

Once the radius r_c has been calculated from condition (4.62), then from $(4.60)_4$ one obtains the distributions of both Martensite variants in the AM region and in the corner region C as the complete Martensitic transformation is achieved at r_i

$$\xi^C_{r\theta}(r) = \frac{1}{\gamma-1}\left[1-2\frac{r_c}{r}+\frac{\gamma}{\delta}\left(\ln\frac{r_c}{r}+\delta\right)\frac{r_i}{r}\right], \tag{4.63}$$

$$\xi^C_{r3}(r) = \frac{1}{\gamma-1}\left(2\frac{r_c}{r}-2-\frac{\gamma}{\delta}\,\frac{r_i}{r}\,\ln\frac{r_c}{r}\right). \tag{4.64}$$

In particular, the volume fractions of both Martensite variants at r_i coincide with those obtained in (4.40).

4.5.2. Start of the martensitic transformation at r_o

The outer austenitic region A vanishes off when $\sigma^{AM}_e(r_o)=\sigma_s$ namely for $r_c=r_3$ where r_3 has been defined in (4.10). According to (4.61) and using (4.32) and (4.10), this situation occurs for $q=q_{10}$ where q_{10} has been defined in (4.33). Therefore, the outer austenitic region A disappears for $q>q_{10}$, whereas a fully martensitic region M appears at r_i for $q=\gamma$. Note from 4 that the solution found in Section 4.5 holds true for $q_{10}\le q\le\min\{\gamma,\ q_d\}$ and if the wall thickness obeys the condition $r_1\le r_i\le r_3$, where r_1 has been defined in (4.52) and corresponds to the condition $q_{10}=\gamma$. For $q<q_{10}$ an outer austenitic region is still present when the corner region takes place at r_i, thus recovering the case examined in Section 3.4.

4.6. Thick-walled cylinder made of a single region (AM)

If $\sigma_\theta(r_i)>0$ and the internal pressure p is larger than $q_1\ \sigma_s$ then the outer austenitic region A vanishes before the complete martensitic transformation is achieved at r_i. In this case, the cylinder wall is formed by a single region AM in a mixture of phases. The unknown constants A_1 and A_2 that appear in the fields (3.9)–(3.13) within the region AM, then follow from the introduction of (3.9) in the conditions $\sigma^{AM}_r(r_i)=-q\ \sigma_s$ and $\sigma^{AM}_r(r_o)=0$ as

$$A_2=-A_1=\frac{r_i^2}{r_o^2-r_i^2}\left(q-\delta\ln\frac{r_o}{r_i}\right). \tag{4.65}$$

The introduction of these constants in Eqs. (3.9)–(3.13) provides the following stress and displacement fields and volume fraction of principal Martensite variant in the region AM

$$\begin{aligned}
\frac{\sigma^{AM}_r(r)}{\sigma_s} &= \frac{r_i^2}{r_o^2-r_i^2}\left(q-\delta\ln\frac{r_o}{r_i}\right)\left(1-\frac{r_o^2}{r^2}\right)+\delta\ln\frac{r}{r_o},\\
\frac{\sigma^{AM}_\theta(r)}{\sigma_s} &= \frac{r_i^2}{r_o^2-r_i^2}\left(q-\delta\ln\frac{r_o}{r_i}\right)\left(1+\frac{r_o^2}{r^2}\right)+\delta\left(1+\ln\frac{r}{r_o}\right),\\
\frac{\sigma^{AM}_e(r)}{\sigma_s} &= \delta+\frac{2\ r_i^2}{r_o^2-r_i^2}\left(q-\delta\ln\frac{r_o}{r_i}\right)\ \frac{r_o^2}{r^2},\\
\frac{u^{AM}_r(r)}{r} &= \frac{\sigma_s}{E}(1-\nu)\left\{\frac{r_i^2}{r_o^2-r_i^2}\left(q-\delta\ln\frac{r_o}{r_i}\right)\left[1+\frac{1+\nu+(1-\nu)\delta}{(1-\delta)(1-\nu)}\ \frac{r_o^2}{r^2}\right]+\delta\ln\frac{r}{r_o}\right\},\\
\xi^{AM}_{r\theta}(r) &= \frac{1}{\gamma-1}\left[\frac{2r_i^2}{r_o^2-r_i^2}\left(q-\delta\ln\frac{r_o}{r_i}\right)\ \frac{r_o^2}{r^2}-1+\delta\right].
\end{aligned} \tag{4.66}$$

The fields (4.66) hold for $\max\{q_1,\ q_d\}\le q\le q_2$ and $r_2\le r\le r_o$, where r_2 will be defined in Eq. (4.69) and q_2 is the normalized pressure that induces a complete martensitic transformation at r_i, i.e. $\xi^{AM}_{r\theta}(r_i)=1$, namely

$$q_2=\frac{\gamma-\delta}{2}\left(1-\frac{r_i^2}{r_o^2}\right)+\delta\ln\frac{r_o}{r_i}, \tag{4.67}$$

according to $(4.66)_5$. If $\max\{q_1,\ q_d\}\le q\le q_2$, then the cylinder wall is formed by a single region AM in a mixture of phases (Fig. 4).

4.6.1. Complete martensitic transformation achieved at r_i

The introduction of (4.67) in Eqs. (4.66) gives the following stress and displacement fields, corresponding to the achievement of the complete martensitic transformation at r_i:

$$\begin{aligned}
\frac{\sigma^{AM}_r(r)}{\sigma_s} &= \frac{\gamma-\delta}{2}\left(\frac{r_i^2}{r_o^2}-\frac{r_i^2}{r^2}\right)-\delta\ln\frac{r_o}{r},\\
\frac{\sigma^{AM}_\theta(r)}{\sigma_s} &= \frac{\gamma-\delta}{2}\left(\frac{r_i^2}{r_o^2}+\frac{r_i^2}{r^2}\right)+\delta(1-\ln\frac{r_o}{r}),\\
\frac{\sigma^{AM}_e(r)}{\sigma_s} &= \delta+(\gamma-\delta)\ \frac{r_i^2}{r^2},\\
\frac{u^{AM}_r(r)}{r} &= \frac{\sigma_s}{2E}(1-\nu)\left\{(\gamma-\delta)\left[1+\frac{1+\nu+(1-\nu)\delta}{(1-\nu)(1-\delta)}\ \frac{r_o^2}{r^2}\right]\ \frac{r_i^2}{r_o^2}+\delta\ln\frac{r^2}{r_o^2}\right\},\\
\xi^{AM}_{r\theta}(r) &= \frac{1}{\gamma-1}\left(\frac{r_i^2}{r^2}-\eta^2\right),
\end{aligned} \tag{4.68}$$

which hold only for $r_i\le r\le r_o$ and $\sigma_\theta>0$. To ensure that the latter condition is met everywhere in the cylinder, it is sufficient to check that the condition $\sigma^{AM}_\theta(r_i)>0$ holds true, namely that $r_i>r_2$, where

$$r_2^2=\frac{\delta\ r_o^2}{\gamma-\delta}\ W_0\left(\frac{\gamma-\delta}{\delta}e^{-1-\frac{\gamma}{\delta}}\right). \tag{4.69}$$

4.7. Thick-walled cylinder composed of three regions (M^*, C, AM)

For thick rings, a Martensite region M^* containing both variants may appear at the inner boundary after the outer Austenite region A disappeared. In this case, the cylinder wall is partitioned into an outer region AM in a mixture of phases for $r_c<r<r_o$, a corner region C for $r_f<r<r_c$, and a Martensite region M^* for $r_i<r<r_f$ (Fig. 3*d*). The radial variation of the stress and displacement fields and Martensite volume fractions within the outer AM region are given by (4.56) in terms of r_c. The relation between the radii r_f and r_c follows from (4.62) by replacing r_i with r_f, namely

$$r_f=-\frac{\delta}{\gamma}\,\frac{r_c\ r_o^2}{r_o^2+r_c^2}\left(1-\frac{r_c^2}{r_o^2}+\ln\frac{r_c^2}{r_o^2}\right), \tag{4.70}$$

where $r_f\ge r_1$ and $r_c\le r_3$. Note that for $r_c=r_3$ Eqs. (4.70) and (4.10) provide $r_f=r_1$. This relation has been plotted in Fig. 6 by dash-dotted line.

The constant C entering the definition of the fields in the intermediate corner region C is given by Eq. (4.41) obtained from the condition $\sigma^C_r(r_f)=-\sigma_f$. Continuity of the volume fraction of the principal Martensite variant across the interface at r_c, namely $\xi^{AM}_{r\theta}(r_c)=\xi^C_{r\theta}(r_c)$, by using (3.19), $(4.56)_5$, (4.41) and (4.70), yields:

$$D=-\frac{r_c\ r_o}{r_c^2+r_o^2}\left(\delta+\ln\frac{r_c}{r_o}\right)\left(1-\frac{r_c^2}{r_o^2}+\ln\frac{r_c^2}{r_o^2}\right)-2\frac{r_c}{r_o}. \tag{4.71}$$

The introduction of constants C and D in Eqs. (3.15), (3.19)–(3.21) then provides the radial variation of the fields within the corner region C in terms of the radii r_c and r_f.

$$\begin{aligned}
\frac{\sigma^C_r(r)}{\sigma_s} &= \frac{\delta\ r_o^2}{r_c^2+\ r_o^2}\left(1-\frac{r_c^2}{r_o^2}+\ln\frac{r_c^2}{r_o^2}\right)\frac{r_c}{r},\\
\xi^C_{r\theta}(r) &= \frac{1}{\gamma-1}\left[1-2\frac{r_c}{r}-\left(1-\frac{r_c^2}{r_o^2}+\ln\frac{r_c^2}{r_o^2}\right)\right.\\
&\qquad\left.\left(\delta+\ln\frac{r_c}{r}\right)\frac{r_o^2}{r_c^2+\ r_o^2}\,\frac{r_c}{r}\right],\\
\xi^C_{r3}(r) &= \frac{1}{\gamma-1}\left[2\frac{r_c}{r}-2+\left(1-\frac{r_c^2}{r_o^2}+\ln\frac{r_c^2}{r_o^2}\right)\ \frac{r_o^2}{r_c^2+\ r_o^2}\ \ \frac{r_c}{r}\ \ln\frac{r_c}{r}\right],\\
\frac{u^C_r(r)}{r} &= \frac{\sigma_s}{E}\,\frac{\delta}{1-\delta}\left[1-2\frac{r_c}{r}-\left(1-\frac{r_c^2}{r_o^2}+\ln\frac{r_c^2}{r_o^2}\right)\right.
\end{aligned}$$

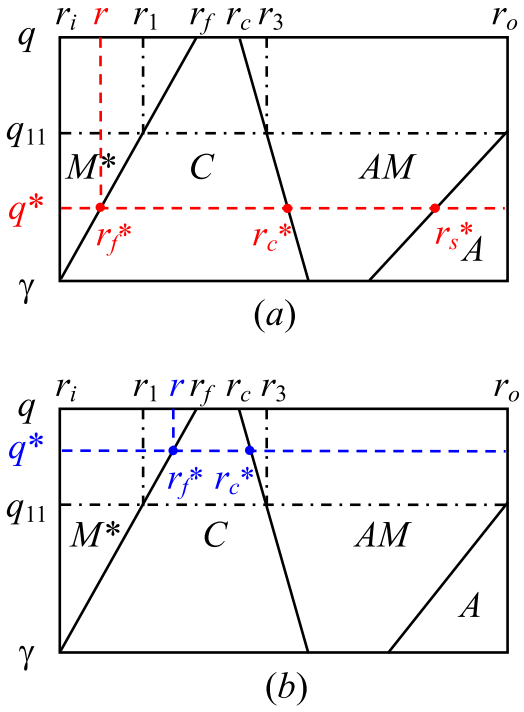

Fig. 8. Sketch and definition of radii r_f^*, r_c^* and r_s^* as functions of r, for $r_i < r < r_1$ (a) and $r_1 < r < r_f$ (b), for the (M^*,C, AM) phase partitioning.

$$\left(\delta + \nu - \nu\delta - \ln\frac{r}{r_c}\right)\frac{r_o^2}{r_c^2 + r_o^2}\frac{r_c}{r}\Bigg]. \tag{4.72}$$

The stress and displacement fields in the inner Martensite region M^* then follow from Eqs. (4.46), where the function $\xi_{r\theta}^M(r)$ has been defined in (4.47) in terms of the parameter r_c^*. The latter parameter is defined as an implicit function of r according to two different situations concerning the cylinder wall partition sketched in Fig. 8. Indeed, for $r_i \le r \le r_1$ then the outer austenitic region A was still present in the outer part of the cylinder wall when the finish martensitic transformation occurred at r under the normalized pressure q^* (Fig. 8a), namely for $r_f^* = r$. Then $r_s^* < r_o$ and $r_c^* < r_3$ and $r_{lim} < r = r_f^*$, so that r_c^* is given by Eq. (4.48)$_2$. Otherwise, for $r_1 \le r \le r_f$ the outer region A has already disappeared when the finish martensitic transformation occurred at r (Fig. 8b). In this case, $r_c^* > r_3$ and r_c^* is given by Eq. (4.62) written for $r_i = r$ and $r_c = r_c^*$, namely

$$r = -\frac{\delta}{\gamma}\frac{r_c^* r_o^2}{r_o^2 + r_c^{*2}}\left(1 - \frac{r_c^{*2}}{r_o^2} + \ln\frac{r_c^{*2}}{r_o^2}\right), \tag{4.73}$$

for $r_1 < r < r_2$. The radii r_1, r_2 and r_3 have been defined in (4.52), (4.69) and (4.10), respectively.

Once the distribution of Martensite variants inside the martensitic region M^* has been defined by the functions $\xi_{r\theta}^M(r)$ and $\xi_{r3}^M(r) = 1 - \xi_{r\theta}^M(r)$, then the radius r_f can be obtained from the relation $q = Q(r_f)$ as an implicit function of the normalized pressure q. Finally, the radius r_c can be found from relation (4.70).

4.7.1. Disappearing of the corner region c between M^* and AM regions

For very thick rings with $r_i \le r_2$, the corner region C may disappear when $r_f = r_c$, namely for $r_f = r_2$ according to (4.69) and (4.70). The corresponding pressure q_{d2} follows from the condition

$$q_{d2} = Q(r_2), \tag{4.74}$$

where the function $Q(r)$ has been defined in Section 4.4 and the condition $\xi_{r\theta}^M(r_2) = 1$ must be considered.

4.8. Thick-walled cylinder composed of two regions (M, AM)

Let us first consider the case of the wall thickness partitioned in an outer region AM in a mixture of phases and in a fully martensitic inner region M containing only the principal Martensite variant (Fig. 3c). This situation occurs for $r_i > r_2$, where r_2 has been defined in (4.69) as the radius of the front of finish martensitic transformation when the martensitic transformation starts at r_o. Then, the unknown constants entering the stress and displacement fields are A_1, A_2, B_1 and B_2. These unknowns can be found by imposing the conditions

$$\sigma_r^{AM}(r_o) = 0,\ \ \sigma_e^{AM}(r_f) = \sigma_f,\ \ \sigma_r^{M}(r_f) = \sigma_r^{AM}(r_f),\ \ \sigma_e^{M}(r_f) = \sigma_f, \tag{4.75}$$

requiring the vanishing of radial stress at r_o and the continuity of the radial and effective stresses through the fronts of start and finish martensitic transformations at r_f. By using Eqs. (3.9), (3.11), (3.25) and (3.28), conditions (4.75) provide the following constants

$$A_1 = -\frac{\gamma - \delta}{2}\frac{r_f^2}{r_o^2},\quad A_2 = \frac{\gamma - \delta}{2}\frac{r_f^2}{r_o^2}, \tag{4.76}$$

$$B_1 = -\frac{\gamma - \delta}{2(1-\delta)}\frac{r_f^2}{r_o^2},\ \ B_2 = \frac{\gamma - \delta}{2}\left[\frac{\delta}{1-\delta}\left(1 + \ln\frac{r_f^2}{r_o^2}\right) + \frac{r_f^2}{r_o^2}\right]. \tag{4.77}$$

The introduction of the constants A_1 and A_2 in (3.9)–(3.13) yields the following fields within the outer region AM in a mixture of phases in terms of r_f:

$$\begin{aligned}
&\tfrac{\sigma_r^{AM}(r)}{\sigma_s} = \tfrac{\gamma-\delta}{2}\tfrac{r_f^2}{r_o^2}\left(1 - \tfrac{r_o^2}{r^2}\right) + \delta\ln\tfrac{r}{r_o},\\
&\tfrac{\sigma_\theta^{AM}(r)}{\sigma_s} = \tfrac{\gamma-\delta}{2}\tfrac{r_f^2}{r_o^2}\left(1 + \tfrac{r_o^2}{r^2}\right) + \delta\left(1 + \ln\tfrac{r}{r_o}\right),\\
&\tfrac{\sigma_e^{AM}(r)}{\sigma_s} = \delta + (\gamma-\delta)\tfrac{r_f^2}{r^2},\\
&\tfrac{u_r^{AM}(r)}{r} = \tfrac{(1-\nu)}{2}\tfrac{\sigma_s}{E}\left\{(\gamma-\delta)\left[\tfrac{r_f^2}{r_o^2} + \tfrac{1+\nu+(1-\nu)\delta}{(1-\nu)(1-\delta)}\tfrac{r_f^2}{r^2}\right] - \delta\ln\tfrac{r_o^2}{r^2}\right\},\\
&\xi_{r\theta}^{AM}(r) = \tfrac{1}{\gamma-1}\left[(\gamma-\delta)\tfrac{r_f^2}{r^2} - 1 + \delta\right],
\end{aligned} \tag{4.78}$$

which hold for $r_f \le r \le r_o$. Moreover, the introduction of B_1 and B_2 in (3.25)–(3.29) gives the stress and displacement fields within the inner martensitic region M in terms of r_f:

$$\begin{aligned}
&\frac{\sigma_r^M(r)}{\sigma_s} = \frac{\delta}{2}\left[\eta^2\left(1 + \ln\frac{r_f^2}{r_o^2} + \frac{1-\delta}{\delta}\frac{r_f^2}{r_o^2} - \frac{r_f^2}{r^2}\right) + \left(\eta^2 - 1\right)\ln\frac{r_o^2}{r^2}\right],\\
&\frac{\sigma_\theta^M(r)}{\sigma_s} = \tfrac{\delta}{2}\left[\eta^2\left(\tfrac{1-\delta}{\delta}\tfrac{r_f^2}{r_o^2} + \tfrac{r_f^2}{r^2} - 1 + \ln\tfrac{r_f^2}{r^2}\right) + 2 - \ln\tfrac{r_o^2}{r^2}\right],\\
&\frac{\sigma_e^M(r)}{\sigma_s} = \left(1 - \eta^2\right)\delta + \tfrac{r_f^2}{r^2}\eta^2,\\
&\tfrac{u_r^M(r)}{r} = \tfrac{\sigma_s}{E}\tfrac{1-\nu}{2}\delta\eta^2\left(\tfrac{1-\delta}{\delta}\tfrac{r_f^2}{r_o^2} + \tfrac{1+\nu}{1-\nu}\tfrac{r_f^2}{\delta\, r^2} + 1 + \ln\tfrac{r_f^2}{r^2} - \tfrac{1}{\eta^2}\ln\tfrac{r_o^2}{r^2}\right).
\end{aligned}$$

which hold for $r_i \le r \le r_f$. Finally, by using (4.79)$_1$ the boundary condition on the internal pressure $\sigma_r^M(r_i) = -q\,\sigma_s$ provides the following relation between the normalized pressure q and the radius r_f

$$q = \frac{\eta^2}{2}\left[\frac{r_f^2}{r_i^2} - \frac{r_f^2}{r_o^2} + \delta\left(\frac{r_f^2}{r_o^2} - 1 - \ln\frac{r_f^2}{r_i^2} + \frac{1}{\eta^2}\ln\frac{r_o^2}{r_i^2}\right)\right], \tag{4.80}$$

which hold for $\max\{r_i,\ r_2\} \le r_f \le r_o$.

4.9. Thick-walled cylinder composed of three regions (M^*, M, AM)

Let us now consider the case of the wall thickness partitioned in an outer region AM in a mixture of phases for $r_f \le r \le r_o$, an intermediate martensitic region M containing the principal Martensite variant for $r_2 \le r \le r_f$, and a fully martensitic inner region M^*

Please cite this article as: E. Radi, Evolution of multiple Martensite variants in a SMA thick-walled cylinder loaded by internal pressure, International Journal of Solids and Structures (2018), https://doi.org/10.1016/j.ijsolstr.2018.06.034

containing both Martensite variants for $r_i \le r \le r_2$ (Fig. 3g). Such a configuration occurs for $r_i < r_2$ and $q > q_{d2}$ after that a corner region took place for $q = q_c$ and then disappeared from the cylinder wall for $q = q_{d2}$ and $r_f = r_2$, leaving a definite amount of secondary Martensite variant within the M^* region. The corresponding stress and displacement fields in the AM and M regions are given by relation (4.78) and (4.79), respectively, in terms of r_f.

The constants C_1 and C_2 defining the stress and displacement fields (3.31)-(3.33) within the inner martensitic region M^* can be found by imposing the continuity of the stress components σ_r^M and σ_θ^M at $r = r_2$ between the martensitic region M^* and the surrounding region M. By using Eqs. (3.31), (3.32) and $(4.79)_{1,2}$, the latter conditions provide

$$C_1 = -\frac{\gamma-\delta}{2}\frac{r_f^2}{r_o^2} - \frac{\delta}{2}\left(1+\ln\frac{r_f^2}{r_o^2}\right), \quad C_2 = \frac{\gamma}{2}\, r_f^2. \tag{4.81}$$

Then, the stress and displacement fields within the martensitic region M^* are derived from Eqs. (3.31)–(3.33) and the condition $\xi_{r\theta}^M(r)=1$ for $r_2 \le r \le r_f$, namely

$$\begin{aligned}
\frac{\sigma_r^M(r)}{\sigma_s} &= \frac{\delta}{2}\left\{(\eta^2-1)\left[\frac{3}{2} - \frac{2r_f^2+r_2^2}{2\,r^2} + \ln\frac{r_f^2}{r_2 r} + \int_r^{r_2}\left(\frac{1}{t}+\frac{t}{r^2}\right)\xi_{r\theta}^M(t)\,dt\right] + 1 - \frac{r_f^2}{r_o^2} + \ln\frac{r_f^2}{r_o^2}\right\} \\
&\quad + \frac{\gamma}{2}\left(\frac{r_f^2}{r_o^2} - \frac{r_f^2}{r^2}\right), \\
\frac{\sigma_\theta^M(r)}{\sigma_s} &= \frac{\delta}{2}\left\{(\eta^2-1)\left[\frac{1}{2} - 2\xi_{r\theta}^M(r) + \frac{2r_f^2+r_2^2}{2\,r^2} + \ln\frac{r_f^2}{r_2\, r} + \int_r^{r_2}\left(\frac{1}{t}-\frac{t}{r^2}\right)\xi_{r\theta}^M(t)dt\right] + 1 - \frac{r_f^2}{r_o^2} + \ln\frac{r_f^2}{r_o^2}\right\} \\
&\quad + \frac{\gamma}{2}\left(\frac{r_f^2}{r_o^2} + \frac{r_f^2}{r^2}\right), \\
\frac{u_r(r)}{r} &= \frac{\sigma_s}{E}\left\{\delta(\eta^2-1)\left[\frac{1-3\nu}{2} - \xi_{r\theta}^M(r) + (1+\nu)\frac{2\,r_f^2+\,r_2^2}{2\,r^2} + (1-\nu)\,\ln\frac{r_f^2}{r\,r_2} + \int_r^{r_2}\left(\frac{1-\nu}{t} - \frac{1+\nu}{r^2}t\right)\xi_{r\theta}^M(t)\,dt\right]\right. \\
&\quad \left. + \frac{1-\nu}{2}\left[\delta\left(1-\frac{r_f^2}{r_o^2}+\ln\frac{r_f^2}{r_o^2}\right) + \gamma\,\frac{r_f^2}{r_o^2}\right] + \gamma\,\frac{1+\nu}{2}\,\frac{r_f^2}{r^2}\right\}.
\end{aligned} \tag{4.82}$$

The function $\xi_{r\theta}^M(r)$ is given by relation (4.47) for $r_i \le r \le r_2$, where the parameter r_c^* is defined as an implicit function of r according to two different situations sketched in Fig. 9. For $r_1 \le r_i$ the outer austenitic region A disappeared from the cylinder wall before the finish martensitic transformation occurred at r_i (Fig. 9a). In this case, the radius r_c^* is defined by Eq. (4.73) as an implicit function of r. In the other case, namely for $r_i < r_1$, the outer austenitic region A was still present in the cylinder wall when the finish martensitic transformation occurred at r_i for $q = \gamma$ (Fig. 9b). In this case, r_c^* is defined as an implicit function of r by Eq. $(4.48)_2$ for $r_i \le r \le r_1$ or by Eq. (4.73) for $r_1 \le r \le r_2$.

Moreover, by requiring that the radial stress at r_i must coincide with the internal pressure, namely $\sigma_r^M(r_i) = -q\,\sigma_s$, then from $(4.82)_1$ it follows

$$\begin{aligned}
q = -\frac{\delta}{2}\left\{(\eta^2-1)\left[\frac{3}{2} - \frac{r_2^2}{2\,r_i^2} + \ln\frac{r_f^2}{r_2 r_i} + \int_{r_i}^{r_2}\left(\frac{1}{t}+\frac{t}{r_i^2}\right)\xi_{r\theta}^M(t)\,dt\right]\right. \\
\left. + \,1 + \ln\frac{r_f^2}{r_o^2}\right\} - \frac{\eta^2}{2}\left[(1-\delta)\frac{r_f^2}{r_o^2} - \frac{r_f^2}{r_i^2}\right],
\end{aligned} \tag{4.83}$$

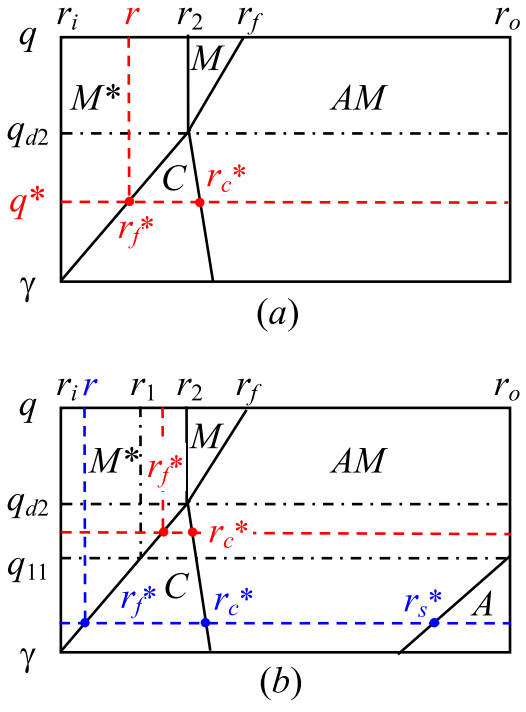

Fig. 9. Sketch and definition of radii r_f^*, r_c^* and r_s^* as functions of r, for $r_1 < r_i < r_2$ (a) and for $r_i < r_1$ (b), for the (M^*, M, AM) phase partitioning.

for $q \ge q_{2d}$.

4.10. Complete martensitic transformation achieved at r_o

The complete martensitic transformation is achieved at r_o when $r_f = r_o$. In this case, the cylinder wall is entirely formed by a purely martensitic region M and Eq. (4.79) provide the corresponding stress and displacement fields:

$$\begin{aligned}
\frac{\sigma_r^M(r)}{\sigma_s} &= \frac{1}{2}\left[\eta^2\left(1-\frac{r_o^2}{r^2}\right) + \delta(\eta^2-1)\ln\frac{r_o^2}{r^2}\right], \\
\frac{\sigma_\theta^M(r)}{\sigma_s} &= \frac{1}{2}\left[\eta^2\left(1+\frac{r_o^2}{r^2}\right) - \delta(\eta^2-1)\left(2-\ln\frac{r_o^2}{r^2}\right)\right], \\
\frac{\sigma_e^M(r)}{\sigma_s} &= \eta^2\,\frac{r_o^2}{r^2} - \delta\,(\eta^2-1), \\
\frac{u_r^M(r)}{r} &= \frac{\sigma_s}{E}\,\frac{1-\nu}{2}\left[\eta^2\left(1+\frac{1+\nu}{1-\nu}\,\frac{r_o^2}{r^2}\right) + \delta(\eta^2-1)\ln\frac{r_o^2}{r^2}\right],
\end{aligned} \tag{4.84}$$

which hold for $r_i \le r \le r_o$. This condition occurs for the pressure $p = q_3\,\sigma_s$, where q_3 is given by relation (4.80) written for $r_f = r_o$, namely

$$q_3 = \frac{1}{2}\left[\eta^2\left(\frac{r_o^2}{r_i^2}-1\right) - \delta(\eta^2-1)\ln\frac{r_o^2}{r_i^2}\right]. \tag{4.85}$$

Then, the stress and displacement increments $\Delta\sigma_r$, $\Delta\sigma_\theta$ and Δu_r corresponding to a further pressure increment $\Delta p = \Delta q\,\sigma_s$ can be obtained from the classical Lamé solution of two-dimensional linear elasticity, namely:

$$\begin{aligned}
\frac{\Delta\sigma_r(r)}{\sigma_s} &= \frac{r_i^2}{r_o^2 - r_i^2}\left(1-\frac{r_o^2}{r^2}\right)\Delta q, \\
\frac{\Delta\sigma_\theta(r)}{\sigma_s} &= \frac{r_i^2}{r_o^2 - r_i^2}\left(1+\frac{r_o^2}{r^2}\right)\Delta q, \\
\frac{\Delta u_r(r)}{r} &= \frac{1+\nu}{E}\,\frac{r_i^2}{r_o^2 - r_i^2}\left(\frac{1-\nu}{1+\nu} + \frac{r_o^2}{r^2}\right)\Delta q\;\sigma_s.
\end{aligned} \tag{4.86}$$

Please cite this article as: E. Radi, Evolution of multiple Martensite variants in a SMA thick-walled cylinder loaded by internal pressure, International Journal of Solids and Structures (2018), https://doi.org/10.1016/j.ijsolstr.2018.06.034

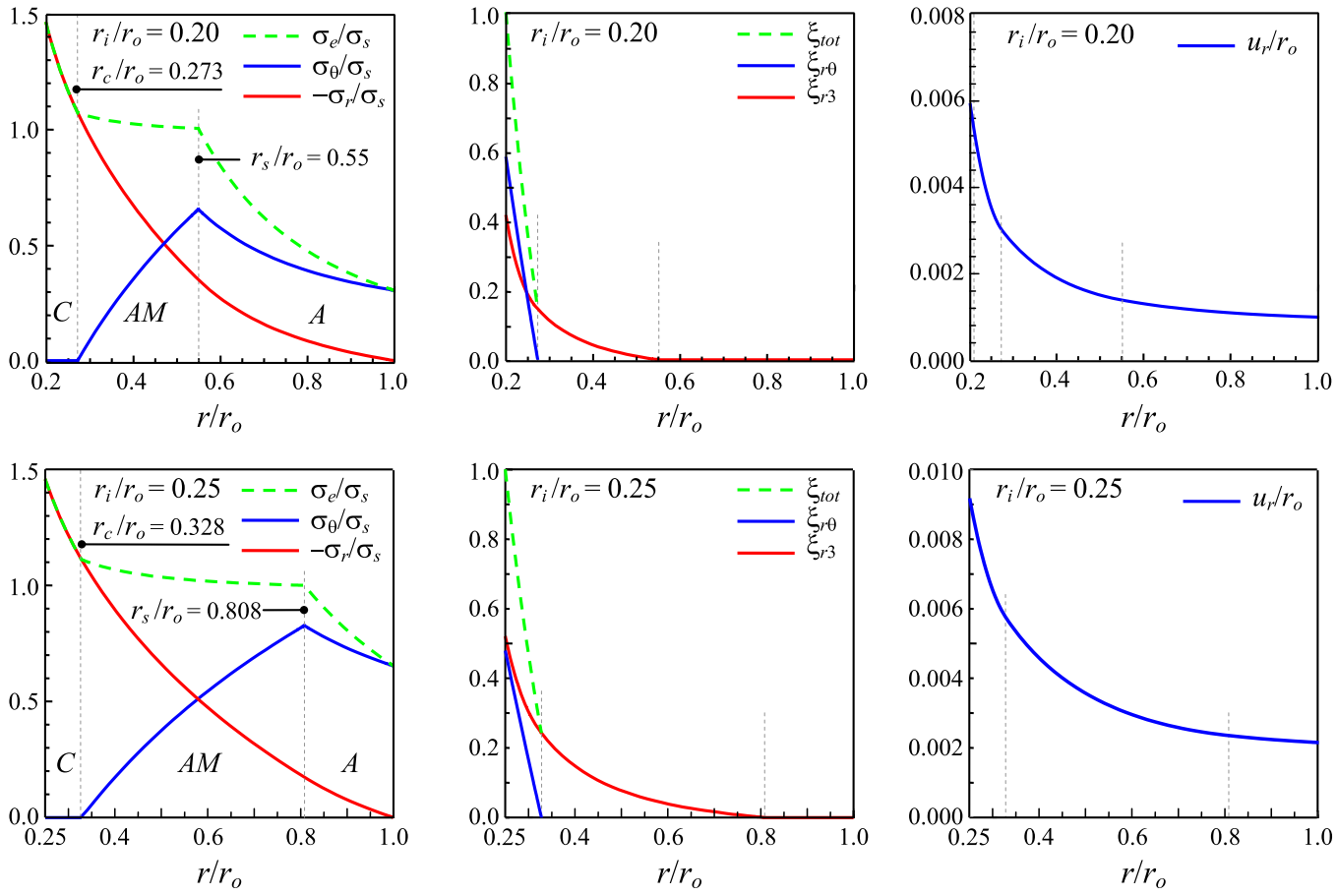

Fig. 10. Variation of stresses, Martensite fractions and radial displacement within the thickness in thick-walled cylinders as the complete martensitic transformation is achieved at the inner radius, namely for $q = \gamma$.

Table 2
Non-dimensional parameters for SMA materials BL and TA.

	BL	TA
δ	0.9781	0.9334
γ	1.4575	1.1667
η	4.6782	1.8719
r_1/r_o	0.2658	–
r_2/r_o	0.2823	–
r_3/r_o	0.3278	–
r_4/r_o	0.3324	–
r_{lim}/r_o	0.2599	–
r_a/r_o	–	0.0331
r_b/r_o	–	0.5342

5. Results

The variations of the pressure delimiting the admissible partitions of the cylinder wall with the ratio r_i/r_o are plotted in Figs. 4 and 5 for the sets BL and TA of the constitutive parameters, respectively. These curves single out the regions in the plane q vs r_i/r_o where the different types of partitioning take place during the loading process. These figures provide simple maps for finding the internal pressure required to produce a desired phase partitioning for every assigned cylinder geometry, that may be useful for the design of device control systems realized by means of SMA cylinders and tubes.

The material parameters defined in (3.7), (3.14) and (4.11) for the SMA materials BL and TA are reported in Table 2, together with the normalized values of the radii r_1, r_2, r_3, r_4, r_{lim}, r_a and r_b separating the admissible phase partitioning within the wall thickness reported in Figs. 4 and 5 and defined by Eqs. (4.52), (4.69), (4.10), (4.17), (4.39) and (4.13), respectively.

For the BL set of constitutive parameters, the curve denoted with q_2 in Figs. 4*a* and 5*a* provides the normalized internal pressure required for the achievement of a complete martensitic transformation at r_i for a relatively thin cylinder wall with $r_i \geq r_2$. From Fig. 4a it can be observed that the pressure q_2 increases with the wall thickness, namely as the ratio r_i/r_o decreases, and it reaches the value γ for $r_i = r_2$. The same pressure $q = \gamma$ is required to complete the martensitic transformation at r_i also for thicker cylinder walls.

The curves denoted with q_1, q_{10} and q_{11} in F define the normalized pressure required for starting the martensitic transformation at r_o. Therefore, the outer austenitic region A disappears for larger pressure. The curves denoted with q_c, q_{d1}, q_d, and q_{d2} in the same figures delimit the region in the plane q vs r_i/r_o where the corner region C takes place within the cylinder wall. The secondary Martensite variant is produced within this region only, whose maximum extension is r_4.

The curves plotted in Fig. 5 for the TA set of constitutive parameters show that the pressures q_1 and q_2 become coincident for $r = r_b$, so that the special partition with the cylinder wall made of the single region (AM) may occur only for $r_i > r_b$. It may be observed in Fig. 5*b* that the secondary Martensite variant is produced only for very thick-walled cylinders satisfying $r_i \ \langle < r_a$, for $q \rangle > q_c$. Therefore, the results provided by Tabesh et al. (2013) by neglecting the formation of the secondary Martensite variant are accurate for $r_i > r_a$, for the particular TA set considered there.

The results plotted in Figs. 10–16 concern only the BL set of constitutive parameters. In particular, the variations of the stress

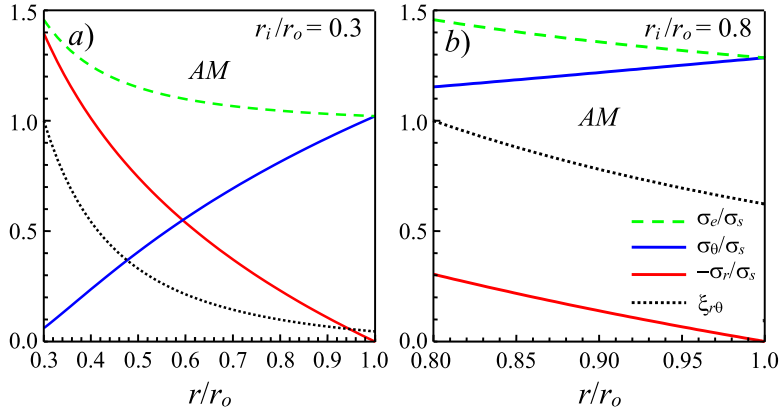

Fig. 11. Variation of stresses and volume fractions of Martensite variants within the thickness in a thin-walled cylinders (a) and in a relatively thick-walled cylinders (b) as the complete martensitic transformation is achieved at r_i, namely for $q = q_2$. In both cases, the cylinder wall is made entirely of a region AM in a mixture of phases.

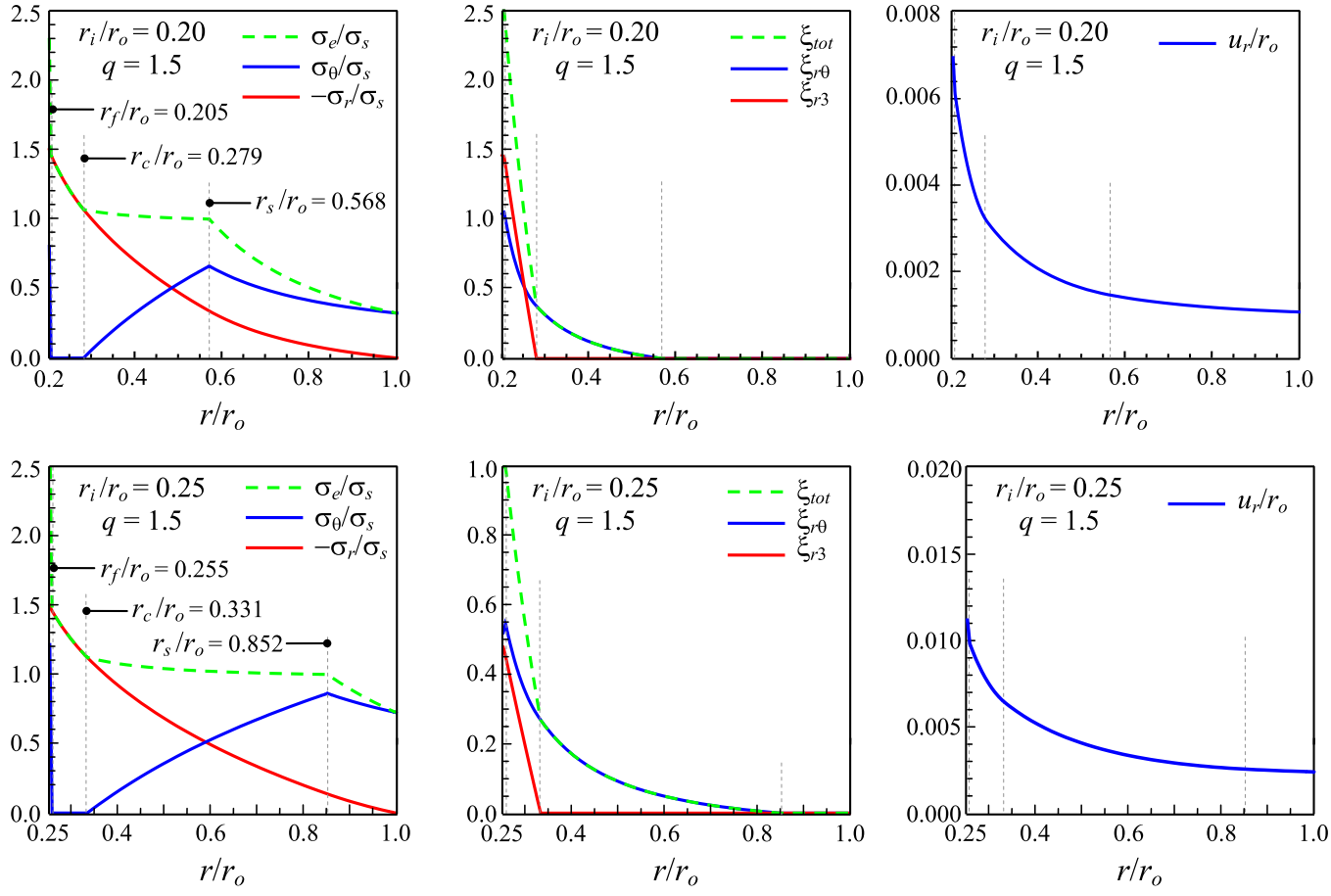

Fig. 12. Distribution of stresses, volume fractions of Martensite variants and radial displacement within the thickness in very thick-walled cylinders a bit after the complete martensitic transformation is achieved at the inner radius.

field, volume fraction of Martensite variants and radial displacement within the wall thickness, corresponding to the achievement of the complete martensitic transformation at r_i under the normalized internal pressure $q = \gamma$, are plotted in Fig. 10 for the geometric ratio r_i/r_o equal to 0.2 and 0.25, both values correspond to very thick wall. From these figures it may be observed that the tangential stress attains a maximum at the front of start Martensite transformation r_s and tends to vanish at the inner radius r_c of the mixed region AM, due to the constraint effect induced by the surrounding austenitic region A, which behaves elastically. As a consequence, a corner region takes place for $r_i \le r \le r_c$, where the secondary Martensite variant starts forming, till the volume fractions of the two variants become comparable. Note that the variation of ξ_{r3} within the wall thickness is proportional to the inelastic axial elongation, according to the constitutive relation $(2.6)_3$. As expected, the magnitude of radial displacement decreases as the wall thickness increases. The variations of the stress field and volume fraction of principal Martensite variant are plotted in Figs. 11a and 11b for thinner cylinder walls, namely for the ratio r_i/r_o equal to 0.3 and 0.8, respectively. In both cases, no secondary Martensite variant is present when the front of finish Martensite transformation reaches the inner radius r_i. It can be observed that for

Please cite this article as: E. Radi, Evolution of multiple Martensite variants in a SMA thick-walled cylinder loaded by internal pressure, International Journal of Solids and Structures (2018), https://doi.org/10.1016/j.ijsolstr.2018.06.034

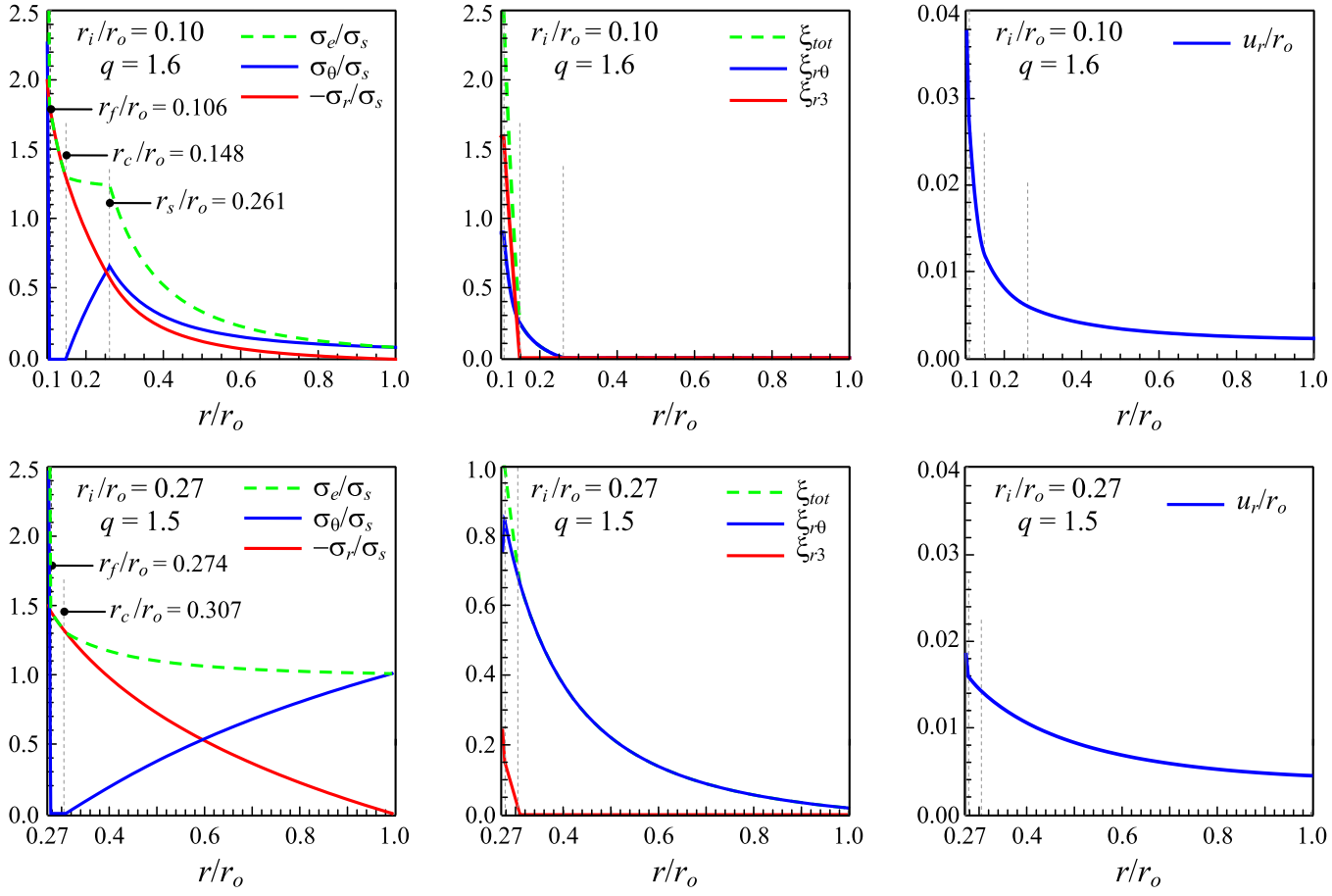

Fig. 13. Variation of stresses, volume fractions of Martensite variants and radial displacement within the thickness in very thick-walled cylinders a bit after the complete martensitic transformation is achieved at the inner radius.

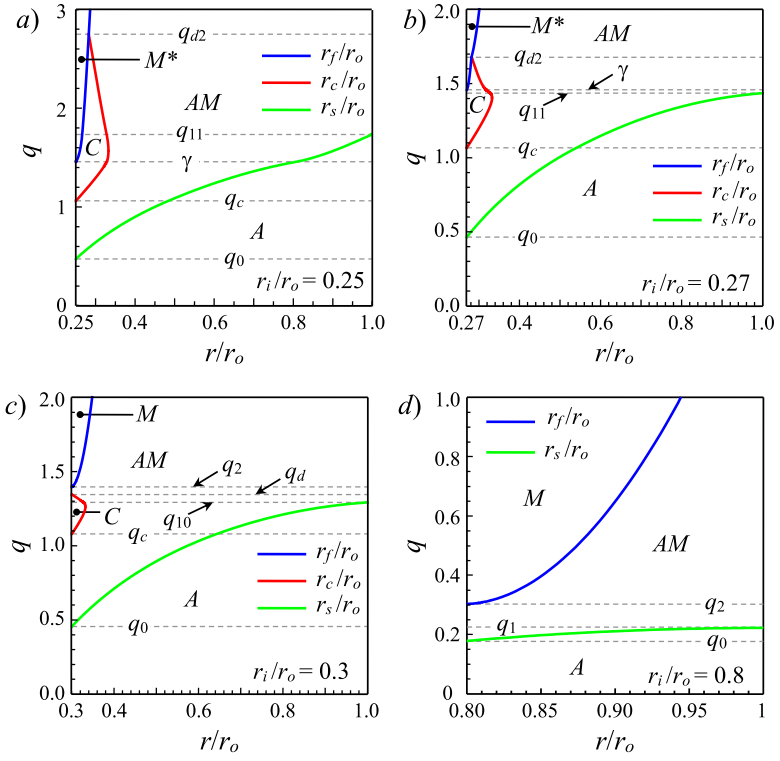

Fig. 14. Variation of the fronts of start and finishing martensitic transformation during the loading process for a very thick-walled cylinder (*a, b, c*). and a relatively thin-walled cylinder (*d*).

Please cite this article as: E. Radi, Evolution of multiple Martensite variants in a SMA thick-walled cylinder loaded by internal pressure, International Journal of Solids and Structures (2018), https://doi.org/10.1016/j.ijsolstr.2018.06.034

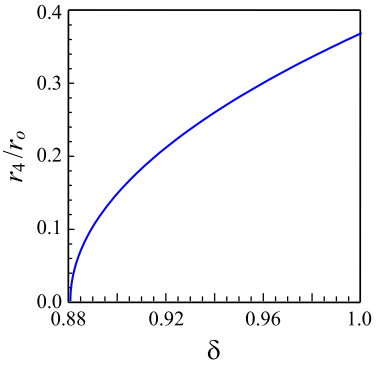

Fig. 15. Variation of the normalized radius r_4 with the material parameter δ.

$r_i/r_o = 0.3$, the tangential stress is near to vanish at the inner radius and a corner region already took place for $q > q_c$ and then disappeared for $q > q_d$, according to the diagram in Fig. 5.

Similar variations are plotted in Figs. 12 and 13 for a small increment of the internal pressure that allows the finish transformation front propagating within the wall thickness, namely for q equal to 1.5 and 1.6, both values being greater than γ. It can be observed that both the tangential stress and the effective Tresca stress increase considerably within the fully martensitic region M^*, so that the yield condition of the SMA could be reached quickly. A similar trend was observed by Mirzaeifar et al. (2012) in their semi-analytical investigations and it must be carefully considered in the design of SMA thick-walled pipe joints. Therefore, in order to avoid severe plastic deformations, the loading process should be interrupted soon after the complete martensitic transformation is achieved at r_i, namely when the internal pressure p attains the threshold value σ_f.

The total Martensite volume fraction is 1 in the inner fully martensitic region M^*. It ranges between 0 and 1 within the corner region C and the region AM in a mixture of phases and it vanishes in the fully austenitic outer region A, which is still present at the end of the loading process only if the wall is very thick.

The variations of the fronts of start and finish martensitic transformations, defined by the radii r_s, r_c and r_f, with the normalized internal pressure $q = p/\sigma_s$ are plotted in Fig. 14 for relatively small and large wall thickness. These plots provide the actual variations of the radii separating the different annular region that are sketched in Figs. 7–9 in a preliminary form.

The curves plotted in Fig. 14*a,b,c* concern three cases with $r_i < r_4$ where the corner region takes place. These results provide a correction to the predictions obtained by Mirzaeifar et al. (2012) and Tabesh et al. (2013) by neglecting the formation of the secondary Martensite variant. If the wall thickness is very large, e. g. for $r_i = 0.25 r_o < r_1$, Fig. 14*a* shows that the corner region C and the fully martensitic region M^* take place when the outer austenitic region A is still present within the wall thickness. For smaller wall thickness, instead, the fully martensitic region M^* takes place after that the outer austenitic region A has disappeared (see Figs. 14*b,c* for $r_i = 0.27\ r_o < r_2$ and $r_i = 0.3\ r_o < r_3$, respectively). Note that for large wall thickness, namely for $r_i < r_4$, the corner region takes place for a normalized pressure q lower than q_{d2} and it extends up to the radius r_4 for $q = q_4$ Therefore, an accurate analysis for a pressurized thick-walled SMA cylinder with $r_i < r_4$ must necessarily take into account the formation of the secondary Martensite variant. The curve plotted in Fig. 14*d* holds instead for a relatively thin cylinder wall with $r_i > r_4$ and thus it recovers the findings of the previous authors, since no corner region takes place in the cylinder wall in this case.

The variation of the normalized radius r_4/r_o with the material parameter δ is plotted in Fig. 15. For most of SMA materials the parameter δ is close to 1 and, thus, the corner region may appear in thick walled SMA cylinders only if $r_i/r_o < 1/e \approx 0.368$.

The problem of a hole in an infinite plate investigated by Birman (1999) is also recovered by the present analysis as a special

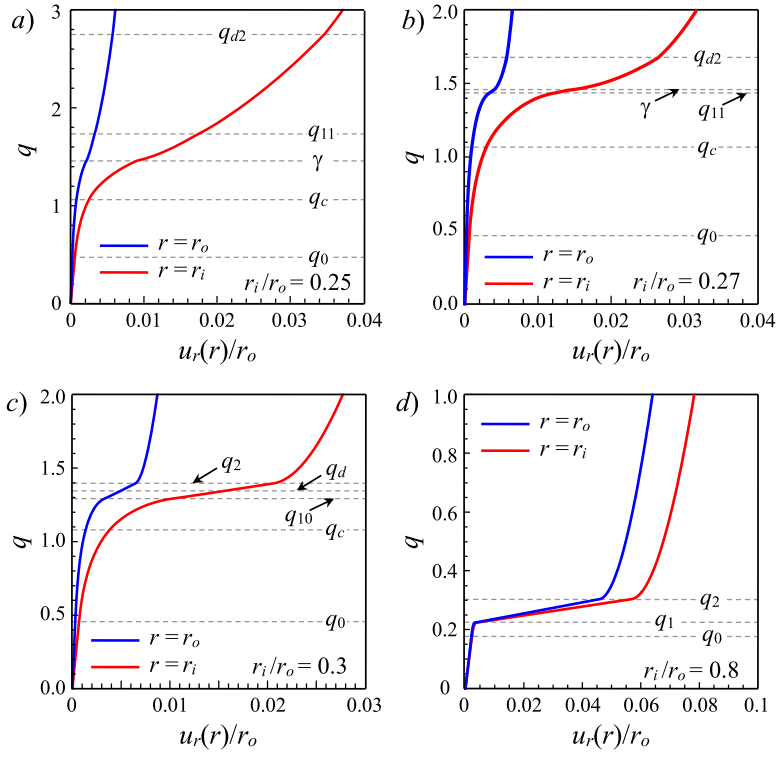

Fig. 16. Variations of the normalized radial displacements at the inner and outer radii of the cylinder wall with the internal pressure for a very thick-walled cylinder (*a, b, c*). and a relatively thin-walled cylinder (*d*).

Please cite this article as: E. Radi, Evolution of multiple Martensite variants in a SMA thick-walled cylinder loaded by internal pressure, International Journal of Solids and Structures (2018), https://doi.org/10.1016/j.ijsolstr.2018.06.034

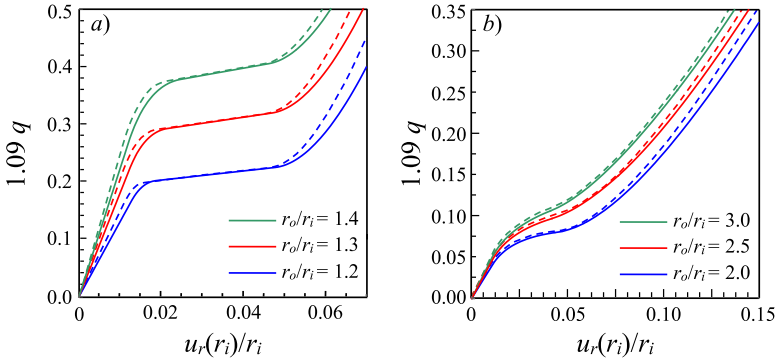

Fig. 17. Variation of normalized radial displacements at the inner radius of the cylinder wall with the internal pressure for a thin-walled cylinder (*a*) and a thick-walled cylinder (*b*). The results obtained in the present analysis for plane stress (solid lines) for a TA material are compared to those obtained by Tabesh et al. (2013) for plane strain (dashed lines).

case for $r_o \to \infty$. In this limit case, from (4.7) and (4.16) it follows

$$q_0 = \frac{1}{2}, \qquad q_c = \delta\left[1 - W_0\left(-\frac{1-\delta}{\delta}e\right)\right]. \tag{5.1}$$

If the plate is initially fully austenitic, then a mixed annular region *AM* appears around the hole for $q = q_0$ and it extends outward. Then, a corner region *C* originates inside the mixed region *AM* for $q = q_c$. Finally, for $q \geq \gamma$ a fully martensitic annular region M^* originates starting from r_i. During this loading process the outer purely austenitic region is always present at increasing distance to the hole.

The variations of the radial displacement u_r normalized by r_o with the normalized internal pressure q are shown in Figs. 16 for the same radii considered in Fig. 14. It can be observed that the radial displacement is always larger at r_i than at r_o, being the pressure applied at r_i. Moreover, the larger displacement rate occurs for $q_c < q < \gamma$, namely when the transformation to both Martensite variants is active. In this case, a significant amount of transformation strain occurs in the axial direction. For $q > \gamma$ most of the inner part of the wall has been transformed to Martensite and is no more available to elongate in the tangential direction by martensitic transformation and thus it displays elastic behavior, whereas in the inner part of the wall thickness the martensitic transformation is still in progress. Therefore, a further increment in the internal pressure will produce a high tensile tangential stress at the inner radius, as detected in Figs. 12 and 13. Moreover, the elastic behavior of the inner Martensite region results in a stiffening effect as the internal pressure is further increased, as it can be observed in Fig. 16 for large internal pressure. Note also that the response is linear between the normalized pressures q_d and q_2 in Fig. 16*c* and between q_1 and q_2 in Fig. 16*d*, being the wall composed of a single region *AM* in a mixture of phases within these ranges of pressure, in agreement with the observations of Tabesh et al. (2013).

It must be remarked that the present results hold for plane stress loading condition. They are expected to hold qualitatively for the radial and tangential stress components also under plane strain loading condition if the condition $\sigma_r \leq \sigma_3 \leq \sigma_\theta$ is attained. In this case, indeed, no significant difference should occur in the radial and tangential stress components under plane stress and plane strain loading conditions, being the Tresca transformation condition independent of the intermediate stress σ_3. However, under plane strain loading conditions the constitutive relations are affected by the axial stress component σ_3 and, thus, the radial displacement u_r and the Martensite fractions $\xi_{r\theta}$ and ξ_{r3} are expected to differ from the corresponding results under plane stress.

In order to validate the present analysis, a comparison with the few results available in the Literature is provided in Fig. 17. In particular, the variations of normalized radial displacements at the inner radius of the cylinder wall with the internal pressure for a thin-walled cylinder (Fig. 17*a*) and a thick-walled cylinder (Fig. 17*b*) obtained by the present analysis for plane stress (solid lines) for a TA material are compared to those obtained by Tabesh et al. (2013) for plane strain (dashed lines). The curves are very close, except that the radial displacement predicted by the present analyses under plane stress loading condition is a bit larger than that obtained by Tabesh et al. (2013) for plane strain, as reasonably expected. Unfortunately, no results are available in the Literature for plane stress obtained by adopting the Tresca transformation condition for SMA.

6. Conclusions

A simple constitutive model has been used for the description of the axisymmetric loading of a pressurized SMA thick-walled cylinder at constant temperature, under plane stress conditions. The model is based on two variants of the Martensite phase fraction, which linearly evolve with the Tresca effective stress, in analogy with the associative flow rule and corner flow theory of plasticity. The rate constitutive model has been integrated under the assumption of proportional loadings. Moreover, the elastic moduli of Austenite and Martensite are assumed to be identical. These simplifying assumptions allowed us to obtain a closed form solution for the stress and displacement fields and the distribution of the Martensite fractions within the cylinder wall during each step of the loading process. The results show that a significant extent of Martensitic transformation occurs in the axial direction for very thick cylinder wall, and thus it can not be recovered during the successive unloading process.

Due to the widespread applications of SMA, the present analytical results are of great importance for the design of innovative mechanical devices such as connectors, seals and clamping components realized by means of SMA rings and tubes. They can be efficiently used also for validating the accuracy of numerical methods usually employed in the modeling of SMA junctions and they are essential for an accurate modeling of the successive unloading process, which will be investigated in a forthcoming paper.

Acknowledgements

Support from the Italian "Gruppo Nazionale di Fisica Matematica" INdAM-GNFM is gratefully acknowledged.

References

Arghavani, J., Auricchio, F., Naghdabadi, R., Reali, A., Sohrabpour, S., 2010. A 3-D phenomenological constitutive model for shape memory alloys under multiaxial loadings. Int. J. Plast. 26, 976–991.

Auricchio, F., Bonetti, E., Scalet, G, Ubertini, F., 2014. Theoretical and numerical modelling of shape memory alloys accounting for multiple phase transformations and Martensite reorientation. Int. J. Plast. 59, 30–54.
Auricchio, F., Lubliner, J., 1997. A uniaxial model for shape memory alloys. Int. J. Solids Struct. 34 (27), 3601–3618.
Bernardini, D., Pence, T.J., 2016. A structured continuum modelling framework for martensitic transformation and reorientation in shape memory materials. Phil. Trans. R. Soc. A 374 (2066), 20150173.
Birman, V., 1999. Analysis of an infinite shape memory alloy plate with a circular hole subjected to biaxial tension. Int. J. Solids Struct. 36, 167–178.
Borden, T., 1990. Shape memory alloy fastener rings. In: Duerig, T.W., Melton, K.N., Stöckel, D., Wayman, C.M. (Eds.), Engineering Aspects of Shape Memory Alloys. Butterworth-Heinemann, London, pp. 158–169.
Borden, T., 1991. Shape-memory alloys: forming a tight fit. Mech. Eng. 113 (10), 67–72.
Brinson, L.C., 1993. One-dimensional constitutive behavior of shape memory alloys: thermomechanical derivation with non-constant material functions and redefined Martensite internal variable. J. Intell. Mater. Syst. Struct. 4 (2), 229–242.
Brinson, L.C., Lammering, R., 1993. Finite element analysis of the behavior of shape memory alloys and their applications. Int. J. Solids Struct. 30 (23), 3261–3280.
Brook, G.B., 1983. Applications of titanium-nickel shape memory alloys. Mater. Design 4 (4), 835–840.
Chi, Y., Pence, T.J., Tsai, H., 2003. Plane stress analysis of a shape memory annular plate subject to surface pressure. J. Phys. IV 112, 245–248.
Chi, Y., Pence, T.J., Tsai, H., 2005. Axisymmetric plane stress states of an annulus subject to displacive shear transformation. ASME J. Appl. Mech. 72, 44–53.
Chi, Y., Pence, T.J., Tsai, H., 2007. Numerical algorithms for cyclic phase transformation hysteresis in a shape memory plate subject to axisymmetric plane stress. Int. J. Numer. Meth. Eng. 69, 1819–1850.
Chirani, S.A., Aleong, D., Dumont, C., McDowell, D., Patoor, E., 2003. Superelastic behavior modeling in shape memory alloys. J. Phys. IV 112, 205–208.
Corless, R.M., Gonnet, G.H., Hare, D.E.G., Jeffrey, D.J., Knuth, D.E., 1996. On the Lambert W Function. Adv. Comp. Math. 5, 329–359.
Durban, D., Kubi, M., 1992. A general solution for the pressurized elastoplastic tube. ASME J. Appl. Mech. 59, 20–26.
Govindjee, S., Kasper, E.R., 1997. A shape memory alloy model for Uranium-Niobium accounting for plasticity. J. Intell. Mater. Syst. Struct. 8, 815–823.
Govindjee, S., Kasper, E.R., 1999. Computational aspects of one-dimensional shape memory alloy modeling with phase diagrams. Comput. Methods Appl. Mech. Eng. 171, 309–326.
Harrison, J.D., Hodgson, D.E., 1976. Use of TiNi in mechanical and electrical connectors. In: Perkins, J. (Ed.), Shape Memory Effects in Alloys. Plenum Press, New York, pp. 517–523.
Jee, K.K., Han, J.H., Jang, W.Y., 2006. A method of pipe joining using shape memory alloys. Mater. Sci. Eng. A (438-440) 1110–1112.
Kapgan, M., Melton, K.N., 1990. Shape memory alloy tube and pipe couplings. In: Duerig, T.W., Melton, K.N., Stöckel, D., Wayman, C.M. (Eds.), Engineering Aspects of Shape Memory Alloys. Butterworth-Heinemann, London, pp. 137–148.
Koiter, W.T., 1953. Stress-strain relations, uniqueness and variational theorems for elastic-plastic materials with a singular yield surface. Quart. Appl. Math. 11 (3), 350–354.
Kosel, F., Videnic, T., 2007. Generalized plasticity and uniaxial constrained recovery in shape memory alloys. Mech. Adv. Mater. Struct. 14 (1), 3–12.
Lagoudas, D., Hartl, D., Chemisky, Y., Machado, L., Popov, P., 2012. Constitutive model for the numerical analysis of phase transformation in polycrystalline shape memory alloys. Int. J. Plast. 32, 155–183.
Leclercq, S., Lexcellent, C., 1996. A general macroscopic description of the thermomechanical behaviour of shape memory alloys. J. Mech. Phys. Solids 44 (6), 953–980.
Liang, C., Rogers, C.A., 1990. One-dimensional thermomechanical constitutive relations for shape memory materials. J. Intell. Mater. Syst. Struct. 1 (2), 207–234.
Liu, B., Du, C., 2014. Effects of external pressure on phase transformation of shape memory alloy cylinder. Int. J. Mech. Sci. 88, 8–16.
Liu, B., Dui, G., Xue, L., Xie, B., 2013. On macroscopic behaviors of shape memory alloy thick-walled cylinder under combined internal pressure and radial temperature gradient. CMES: Comp. Model. Eng. Sci. 94 (3), 239–260.
Lubliner, J., Auricchio, F., 1996. Generalized plasticity and shape-memory alloys. Int. J. Solids Struct. 1 (2), 207–234.
Luig, P., Bruhns, O.T., 2008. On the modeling of shape memory alloys using tensorial internal variables. Mater. Sci. Eng. A 481-482, 379–383.
Marfia, S., Rizzoni, R., 2013. One-dimensional constitutive SMA model with two Martensite variants: Analytical and numerical solutions. Eur. J. Mech. A/Solids 40, 166–185.
Masri, R., Durban, D., 2007. Cylindrical cavity expansion in compressible Mises and Tresca solids. Eur. J. Mech. Solids A 26, 712–727.
Mirzaeifar, R., Shakeri, M., DesRoches, R., Yavari, A., 2012. A semi-analytic analysis of shape memory alloy thick-walled cylinders under internal pressure. Arch. Appl. Mech. 81, 1093–1116.
Nagaya, K., Hirata, Y., 1992. Analysis of a coupling made of shape memory alloy and its dynamic response due to impacts. J. Vib. Acoust. 114 (3), 297–304.
Niccoli, F., Garion, C., Maletta, C., Sgambitterra, E., Furgiuele, F., Chiggiato, P., 2017. Beam-pipe coupling in particle accelerators by shape memory alloy rings. Mater. Design 114, 603–611.
Panoskaltsis, V.P., Bahuguna, S., Soldatos, D., 2004. On the thermomechanical modelling of shape memory alloys. Int. J. Nonlin. Mech. 39 (5), 709–722.
Piotrowski, B., Ben Zineb, T., Patoor, E., Eberhardt, A., 2012. A finite element–based numerical tool for Ni47Ti44Nb9 SMA structures design: Application to tightening rings. J. Intell. Mater. Syst. Struct. 23 (2), 141–153.
Popov, P., Lagoudas, D.C., 2007. A 3-D constitutive model for shape memory alloys incorporating pseudoelasticity and detwinning of self-accommodated Martensite. Int. J. Plast. 23 (10-11), 1679–1720.
Tabesh, M., Boyd, J., Atli, K.C., Karaman, I., Lagoudas, D.C., 2017. Design, fabrication, and testing of a multiple-actuation shape memory alloy pipe coupler. J. Intell. Mater. Syst. Struct. 1045389X17730922.
Tabesh, M., Liu, B., Boyd, J.G., Lagoudas, D.C., 2013. Analytical solution for the pseudoelastic response of a shape memory alloy thick-walled cylinder under internal pressure. Smart Mater. Struct. 22 (9), 094007.
Videnic, T., Kosel, F., Sajn, V., Brojan, M., 2008. Biaxial constrained recovery in shape memory alloy rings. J. Intell. Mater. Syst. Struct. 19, 861–874.
Wang, L., Rong, L.J., Yan, D.S., Jiang, Z.M., Li, Y.Y., 2005. DSC study of the reverse martensitic transformation behaviour in a shape memory alloy pipe-joint. Intermetallics 13, 403–407.
Zaki, W., 2012. An efficient implementation for a model of Martensite reorientation in martensitic shape memory alloys under multiaxial nonproportional loading. Int. J. Plast. 37, 72–94.

Please cite this article as: E. Radi, Evolution of multiple Martensite variants in a SMA thick-walled cylinder loaded by internal pressure, International Journal of Solids and Structures (2018), https://doi.org/10.1016/j.ijsolstr.2018.06.034